In vivo Measurements of Biophysical Properties of a Heart and Aorta in a Mouse Model of Marfan Syndrome

by

Ling Lee

B.Sc., National Taiwan Normal University, 2011

Thesis Submitted in Partial Fulfillment of the
Requirements for the Degree of
Master of Science

in the
Department of Biomedical Physiology and Kinesiology
Faculty of Science

SIMON FRASER UNIVERSITY

Summer 2014

Approval

Name: **Ling Lee**

Degree: **Master of Science**

Title: ***In vivo Measurements of Biophysical Properties of a Heart and Aorta in a Mouse Model of Marfan Syndrome***

Examining Committee: Chair: Dr. Ruben Peter,
Professor and Associate Dean of Research & Graduate Studies, Faculty of Science

Dr. Glen Tibbits,
Senior Supervisor
Professor and Chair, Department of Biomedical Physiology and Kinesiology

Dr. George Sandor,
Supervisor
Professor, Division of Cardiology, Department of Pediatrics, University of British Columbia

Dr. Damon Poburko,
Supervisor
Assistant Professor, Department of Biomedical Physiology and Kinesiology

Dr. Tom Claydon,
External Examiner
Associate Professor, Department of Biomedical Physiology and Kinesiology

Date Defended/Approved: May 28, 2014

Partial Copyright Licence

Ethics Statement

The author, whose name appears on the title page of this work, has obtained, for the research described in this work, either:

a. human research ethics approval from the Simon Fraser University Office of Research Ethics,

or

b. advance approval of the animal care protocol from the University Animal Care Committee of Simon Fraser University;

or has conducted the research

c. as a co-investigator, collaborator or research assistant in a research project approved in advance,

or

d. as a member of a course approved in advance for minimal risk human research, by the Office of Research Ethics.

A copy of the approval letter has been filed at the Theses Office of the University Library at the time of submission of this thesis or project.

The original application for approval and letter of approval are filed with the relevant offices. Inquiries may be directed to those authorities.

Simon Fraser University Library
Burnaby, British Columbia, Canada

update Spring 2010

Abstract

In Marfan Syndrome (MFS) patients cardiovascular complications are the most life-threatening manifestations and death is often sudden due to aortic dissection and rupture. Echocardiography is critical in the diagnosis and follow-up of MFS patients to detect and evaluate their cardiovascular phenotype. High frequency echocardiography was used to investigate the structural and functional properties on 6- and 12-mo WT and MFS [*Fbn1* (C1039G/+)] mice (n = 8). The data show that Pulse Wave Velocity (PWV) was significantly increased in 6-mo MFS vs. WT (366.6 ± 19.9 vs. 205.2 ± 18.1 cm/s; $p < 0.001$) and 12-mo MFS vs. WT (459.5 ± 42.3 vs. 205.3 ± 30.3 m/s; $p = 0.001$) and the PWV increased directly in proportion to age in MFS mice but not in WT mice. LV mass (3.06 ± 0.16 vs. 2.46 ± 0.09 μm/g; $p = 0.007$) was significantly increased in 6-mo MFS mice compared with WT. We also found a significantly enlarged aortic root, decreased E/A ratio, prolonged isovolumic relaxation time and increased myocardial performance index in MFS mice compared with WT for both age groups. This study shows significant aortic dilation and central aortic stiffness in the MFS mice which are associated with LV hypertrophy, systolic and diastolic dysfunction. Moreover, the symptoms progressed with increasing age from six months to twelve months.

Keywords: Marfan syndrome; echocardiography; pulse wave velocity; age; mouse model

Acknowledgements

First of all, my sincere gratitude goes to my senior supervisor Dr. Glen Tibbits for giving me this opportunity to join his laboratory. It is very kind of him to let me chose the project I like, and share with me his immense knowledge of cardiac research. Because of his encouragement, I felt confident to present my data in BPK research day, ISHR international conference, and eventually finished my final defense successfully. I appreciate all his contributions of time and great thoughts to my thesis work. He is the best and most supportive supervisor I can imagine. I feel very lucky to be a graduate student in his laboratory.

I am appreciative for the assistance given by all of my committee members in this research endeavor. However, I am especially grateful for the input I received from Dr. George Sandor. He taught me how to measure the pulse wave velocity by using ultrasound and helped me understand the nuances of the data. The contribution he made by sharing his expertise in the field of clinical research, statistics and echocardiography were invaluable. I would like to thank another committee member, Dr. Damon Poburko, for sharing his scientific knowledge, critical review and input to my thesis work. I want to thank the external examiner Dr. Tom Claydon for spending time to read my thesis and provide knowledgeable comments and questions.

Special thanks go to Dr. Xiaoye (Helen) Sheng for guidance when I first started working at Child and Family Research Institute (CFRI). She always very helpful in troubleshooting the experiments when they did not go smoothly. Furthermore, she assisted me greating in reviewing the data acquisition and measurement to ensure that our results were reliable. Without her guidance, help and guidance this thesis would not have been possible. In addition, many thanks go to our lab members for their constant support and encouragement. They often helped me practice my presentations and editing my writing. I had a lot of great memories with them in this lab.

Finally I want to thank my parents, my brother, my friends and all the people I love for giving me mental support through this endeavor. I felt blessed to have all these great people around me when I doing my Master's degree. Thank you!

Table of Contents

List of Tables

List of Figures

List of Acronyms

ACE	Angiotensin-converting-enzyme
ARB	Angiotensin II type 1 receptor blocker
BMP	Bone morphogenic proteins
BSA	Body surface area
BW	Body weight
CI	Cardiac index
CO	Cardiac output
ECG	Electrocardiogram
ECM	Extracellular matrix
EF	Ejection fraction
ET	Ejection time
FS	Fractional shortening
HR	Heart rate
IA	Innominate artery
IVCT	Isovolumic contraction time
IVRT	Isovolumic relaxation time
IVS	Interventricular septum
LAP	Latency-associated peptide
LCCA	Left common carotid artery
LLC	Large latent complex
LSA	Left subclavian artery
LTBP	Latent TGF-β-binding protein
LV	Left ventricle
LVAW	Left ventricular anterior wall
LVPW	Left ventricular posterior wall
MFS	Marfan syndrome
MMPs	Matrix metalloproteinases
MPI	Myocardial performance index
MV A	Mitral valve atrial velocity
MV E	Mitral valve early velocity
OCT	Optical coherence tomography

PWV	Pulse wave velocity
SR	Strain rate
SV	Stroke volume
TGF-β1	Transforming growth factor beta 1
Tsp-1	Thrombospondin-1
VTI	Velocity time integral

Chapter 1. Introduction and Background

1.1. Introduction

Marfan syndrome (MFS) is an autosomal-dominant disorder of the connective tissue caused by mutations in the fibrillin-1 (*FBN1*) gene (Faivre, Collod-Beroud et al. 2007). This mutation on chromosome 15 leads to myriad of distinct clinical problems, which are manifested in the skeletal, ocular and cardiovascular systems (Dietz, Cutting et al. 1991).

Fibrillin-1 monomers associate to form complex extracellular microfibrils which form scaffolds for elastic fibers in the aorta and other connective tissues (Dietz, Loeys et al. 2005). Fibrillin-1 is not only a major structural component in the extracellular matrix (ECM), but also plays a crucial role in the sequestration and regulation of the transforming growth factor beta (TGF-β1) to maintain matrix homeostasis (El-Hamamsy and Yacoub 2009). The mutation in fibrillin-1 leads to abnormalities in the structure of the microfibrillar matrix, dysregulation of matrix homeostasis with excess TGF-β1, and abnormal cell-matrix interactions in Marfan patients' heart and aorta. The cardiovascular manifestations include mitral valve prolapse, mitral annular calcification, ascending and descending aortic dilatation and dissection, aortic regurgitation and dilated cardiomyopathy in the absence of severe valvular dysfunction (Keane and Pyeritz 2008).

Echocardiography plays an important role in the diagnosis and follow-up of the MFS patients to detect and evaluate their cardiovascular phenotype (Freed and Schiller 1977, Keane and Pyeritz 2008, Kiotsekoglou, Bajpai et al. 2008, Kiotsekoglou, Saha et al. 2010). Aortic root dilation is the earliest and most common manifestations of cardiovascular Marfan disease, which is defined as the major criteria by the revised Ghent criteria (Table 1.1) (De Paepe, Devereux et al. 1996). In addition to evaluating the structural and functional properties of the heart and aorta, pulse wave (PW) velocity

measurements allow one to estimate the level of aorta stiffness (Bradley, Potts et al. 2005), and strain analysis can be used for detecting deformation of the heart (Angtuaco, Vyas et al. 2012).

While the echocardiogram has been widely used in the clinical examination of Marfan patients, echo evaluations in the well-established Marfan [*Fbn1* (C1039G/+)] mouse model on the heart and aorta have yet to be well characterized. The signs associated with age progression in Marfan mice also need to be examined further. The goal of this study is to investigate the structural and functional properties of the heart and aorta in Marfan mice using high resolution ultrasound. Moreover, we aim to evaluate the progress of this disease in Marfan mice by analyzing two different age groups (six months and twelve months).

We hypothesize that due to the paucity of matrix-incorporated fibrillin-1, Marfan mice should have similar cardiovascular features including aortic root dilation, aortic stiffness, left ventricular deformation abnormalities and diastolic dysfunction as that of the human condition. Furthermore, we hypothesize that Marfan mice will exhibit increased wall thickness and LV mass as a result of increased after-load by the loss of the aortic compliance, and all the features will progress with increasing age.

1.2. Marfan Syndrome

1.2.1. Signs and Symptoms of Marfan Syndrome

Marfan syndrome is an autosomal-dominant disease usually caused by heterozygous mutations in the gene *FBN1* that encodes the connective protein fibrillin-1 (Canadas, Vilacosta et al. 2010). The estimated prevalence of Marfan syndrome is about 1 in 5,000-10,000 people, including men and women of all races and ethnic groups (Pearson, Devereux et al. 2008). Approximately 75% of patients with the classic Marfan syndrome phenotype inherit this disease, and the other 25% of the cases result from *de novo* mutations (Keane and Pyeritz 2008).

Marfan syndrome is named after Antoine Marfan, a French pediatrician who first presented the case of a 5-year-old girl with disproportionately long limbs in 1896 (Keane and Pyeritz 2008). It is hard to diagnose and distinguish Marfan syndrome because it is related to more than 30 different signs and symptoms. According to the US National Marfan Foundation, the Ghent Nosology was revised in 2010 with seven new diagnostic criteria (Table 1.1) (Loeys, Dietz et al. 2010).

Most of the visible signs of Marfan patients are skeletal manifestations, including overgrowth of the long bones and joint laxity (Canadas, Vilacosta et al. 2010). Overgrowth of the ribs can change the shape of sternum into pectus excavatum or pectus carinatum. Arachnodactyly (overgrowth of the fingers) often occurs in Marfan patients. (Yuan and Jing 2010). Scoliosis is a common manifestation of Marfan patients and usually progresses at a faster rate than idiopathic scoliosis (De Paepe, Devereux et al. 1996). Disproportionately long limbs, pes planus (flat feet), vertebral column, and a highly arched and narrow palate are also frequently identified in Marfan patients (Canadas, Vilacosta et al. 2010, Yuan and Jing 2010)

In the ocular system, myopia is the most common ocular feature (Nelson and Maumenee 1982). Lens dislocation and ectopia lentis present in about 60% of affected individuals (Maumenee 1981). Marfan patients have a high risk of retinal detachment, glaucoma, and early cataract formation (Canadas, Vilacosta et al. 2010). In the lungs, apical blebs may be found in Marfan patients and in 4~15% of the cases lead to spontaneous pneumothorax (Wood, Bellamy et al. 1984). In the skin, the most common manifestation is striae atrophicae which usually happens in about 65% of Marfan patients (Cohen and Schneiderman 1989). In the nervous system, dural ectasia is found in a high percentage of patients (Canadas, Vilacosta et al. 2010, Yuan and Jing 2010).

Cardiovascular complications are the most life-threatening manifestations in MFS patients. Progressive dilatation of the aorta, usually maximal at the sinus of Valsalva is associated with aortic valve incompetence and aortic dissection or rupture (Judge and Dietz 2005). The aortic pathology represents the main cause of morbidity and mortality in Marfan syndrome (Canadas, Vilacosta et al. 2010). Other cardiovascular signs are mitral valve prolapse, mitral valve regurgitation, descending aorta dissection, and

dilatation of the main pulmonary artery (Judge and Dietz 2005). Dilated cardiomyopathy in the absence of severe valvular dysfunction may also be found (Freed and Schiller 1977, Canadas, Vilacosta et al. 2010, Yuan and Jing 2010). Sudden death is often due to aortic dissection and rupture in young patients (Canadas, Vilacosta et al. 2010).

Table 1.1. Diagnostic criteria for Marfan syndrome (MFS) according to the revised Ghent nosology (Loeys, Dietz et al. 2010).

Revised Ghent criteria for diagnosis of Marfan syndrome and related conditions	**In the absence of a family history of MFS:** 1. Aortic root Z-score ≥ 2 AND ectopia lentis. 2. Aortic root Z-score ≥ 2 AND an FBN1 mutation 3. Aortic root Z-score ≥ 2 AND a systemic score > 7 points 4. Ectopia lentis AND an FBN1 mutation with known aortic pathology **In the presence of a family history of MFS:** 5. Ectopia lentis 6. Systemic score ≥ 7 7. Aortic root Z-score ≥ 2
Scoring of systemic features	• Wrist AND thumb sign = 3 (wrist OR thumb sign = 1) • Pectus carinatum deformity = 2 (pectus excavatum or chest asymmetry = 1) • Hindfoot deformity = 2 (plain pes planus = 1) • Pneumothorax = 2 • Dural ectasia = 2 • Protrusio acetabuli = 2 • Reduced upper segment/lower segment ratio AND increased arm/height AND no severe scoliosis = 1 • Scoliosis or thoracolumbar kyphosis = 1 • Reduced elbow extension = 1 • Facial features (3/5) = 1 (dolichocephaly, enophthalmos, downslanting palpebral fissures, malar hypoplasia, retrognathia) • Skin striae = 1 • Myopia > 3 diopters = 1 • Mitral valve prolapse = 1

1.2.2. The Pathogenesis of Marfan Syndrome

Marfan syndrome is an autosomal dominant, multisystem disorder resulting from mutations in the fibrillin-1 gene (*FBN1*) located on chromosome 15q15-31 (Dietz, Cutting et al. 1991). The mutations in exons 24–32 tend to predict a more severe phenotype and are associated with neonatal Marfan syndrome (Faivre, Collod-Beroud et al. 2007). The

first mutation in *FBN1* was discovered in 1991, and to date more than 1,000 different *fbn1* mutations have been identified. Most mutations are missense mutations, occur within 1 of 46 tandem repeated epidermal growth factor–like domains, and result in enhanced proteolytic degradation of fibillin-1 (Canadas, Vilacosta et al. 2010).

The fibrillin-1 protein is an important structural component of microfibrils in the extracellular matrix (ECM) surrounding myofibers and is widely distributed in elastic and non-elastic tissues (Faivre, Collod-Beroud et al. 2007). Fibrillin-1 is the major structural microfibrillar component which forms a lattice surrounding elastic fibers in providing mechanical strength to the connective tissue (El-Hamamsy and Yacoub 2009). Furthermore, fibrillin-1 plays an important role in the sequestration and regulation of the activity of growth factors and other microfibrillar proteins in the ECM, such as TGF-β1 (El-Hamamsy and Yacoub 2009).

Originally, a decrease in structural fibrillin-1 that directly contributed to the weakening of the aortic wall was thought to be the main mechanism of aortic dissection and dilation in Marfan patients. However, this hypothesis could not explain the osteopenia, overgrowth of tubular bones, reduced skeletal muscle mass and craniofacial abnormalities (Keane and Pyeritz 2008). An understanding of the molecular mechanisms underlying Marfan syndrome was first brought to light by Dietz *et al*. (2004) using the Marfan mouse model. The mice showed an increased TGF-β1 activity and signalling, leading to variable Marfan syndrome manifestations in the ocular, skeletal, and cardiovascular systems (Judge, Biery et al. 2004). This finding indicates that fibrillin-1 plays a crucial role in regulating the TGF-β1, which is a potent stimulator of fibrosis, inflammation and activation of matrix metalloproteinases (MMPs), particularly MMP2 and 9 (Keane and Pyeritz 2008).

In ECM, TGF-β1 is normally maintained in an inactive form by its binding to the latency-associated peptide (LAP), and then binding to the large latent TGF-β-binding protein (LTBP) to form the large latent complex (LLC). The fibrillin-1 protein keeps the inactive TGF-β1 sequestered by binding to the LTBP (Matt, Schoenhoff et al. 2009). In Marfan syndrome, the serum TGF-β1 concentration is increased due to inadequate sequestration which is caused by the fibrillin-1 mutation. In addition, fibrillin-1 fragments

(PF10) can directly cleave the LTBP–LAP bond, releasing active TGF-β1 (Matt, Schoenhoff et al. 2009). Other signals such as thrombospondin-1 (TSP1), bone morphogenic proteins (BMP), various proteases and changes in local pH can cleave the LAP–TGF-β1 or the LTBP–LLC bonds, leading to the release of the active TGF-β1 in the matrix (El-Hamamsy and Yacoub 2009).

Active TGF-β1 dimers can bind to the TGF-β type II receptor which recruits and phosphorylates TGF-β type I receptors (Gressner, Weiskirchen et al. 2002). The TGF-β type I receptor then recruits and phosphorylates SMAD 2 and 3 which then enter the cell nucleus and induces MMP 2 and 9 expression (Xiong, Meisinger et al. 2012). MMPs constitute a series of zinc-containing enzymes which are capable of ECM degradation mainly through direct proteolysis of its structural components (Xiong, Meisinger et al. 2012). As a consequence, the level of MMP in Marfan patients is increased and it causes degradation of the elastin fibers and other components of the extracellular matrix. This leads to more TGF-β1 being unable to bind with fibrillin-1 thereby worsening the state of the illness (Fig.1.1) (El-Hamamsy and Yacoub 2009, Xiong, Meisinger et al. 2012).

In Marfan patients, the increased TGF-β1 activity is associated with aortic aneurysm, emphysema, bone overgrowth, mitral valve anomalies and dislocated lens (Lindsay and Dietz 2011). To sum up, the combination of increased TGF-β1 activity and products of fibrillin-1 degradation lead to an increased MMP signaling, elastin fragmentation, vascular smooth muscle cell apoptosis, macrophage chemotaxis and inflammation in Marfan patients (Booms, Ney et al. 2006, Guo, Booms et al. 2006, Chaudhry, Cain et al. 2007).

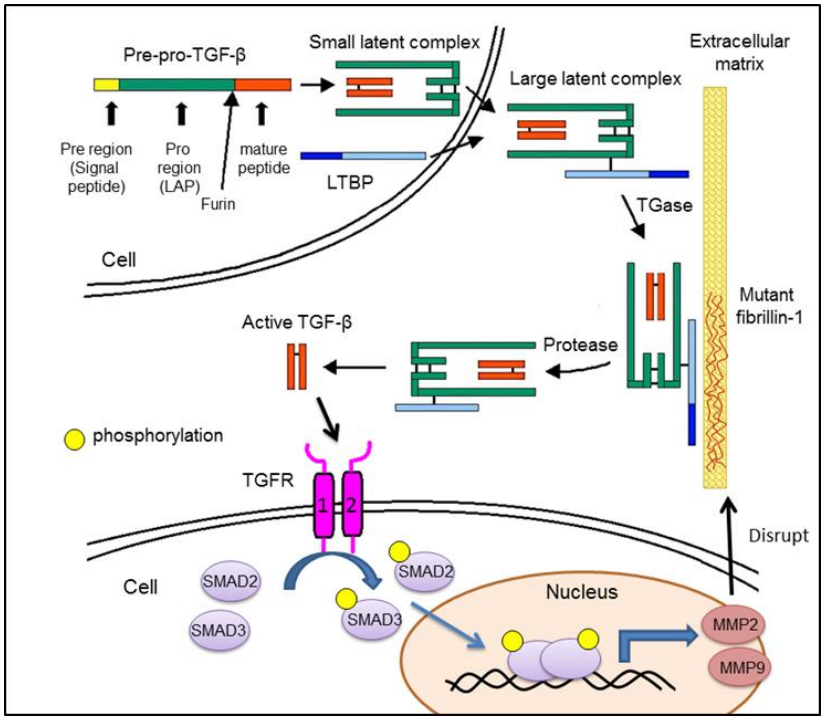

Figure 1.1. TGF-β1 and its downstream signaling pathway in Marfan syndrome (MFS).

The pre-pro-TGF-β1 is a precursor protein that requires a 2-step activation process. At first proteolytic cleavage leads to the elimination of a hydrophobic signal peptide, and a second cleavage leads to cleavage of the pro-region mature peptide. Then the small latent complex is linked to LTBP to form a large latent complex which can be sequestered by fibrillin-1. In MFS, mutant fibrillin-1 causes inadequate sequestration and eventually leads to elevated levels of active TGF-β1. Active TGF-β1 dimers can bind to the TGFR and activate the downstream phosphorylation of SMAD 2/3, which then enters the cell nucleus. SMAD-responsive genes are activated and induce MMP 2/9 expression, which can disrupt the elastic fiber network of blood vessels, resulting in aortic weakness. LAP, latency-associated peptide; LTBP, latent TGF-β1 binding protein; TGase, Tissue transglutaminase; TGFR, TGF-β1 receptors. Figure is modified from (Gressner, Weiskirchen et al. 2002).

1.2.3. Marfan Patient Treatment

Treatment decisions concerning MFS patients depend on the individual manifestations. Marfan syndrome involves several organ systems and thus needs coordinated medical care from specialists in different areas (Arslan-Kirchner, von Kodolitsch et al. 2008). Complete management usually requires a team that includes: a geneticist, a cardiologist, an ophthalmologist, an orthopedist, and cardiothoracic surgeon (Dietz, Loeys et al. 2005).

Since cardiovascular complications are the most life-threatening manifestations in MFS patients, the goal of the treatment generally is to slow the progression of aortic dilation and the damage to the heart valves by eliminating arrhythmias, minimizing the heart rate and the afterload (Canadas, Vilacosta et al. 2010).

A composite aortic valve graft or valve-sparing aortic root replacement surgery becomes necessary if the dilation of the aorta progresses to a significant diameter to prevent dissection or rupture of the aorta (Canadas, Vilacosta et al. 2010). Conventional treatment dictates that when the maximum diameter of the aorta exceeds 5.0 cm, surgical repair is needed (Keane and Pyeritz 2008). In addition to absolute aortic dimensions, the rate of aortic diameter increase approaching 1.0 cm per year or progressive aortic regurgitation occurs also needs surgical repair of the aorta (Judge and Dietz 2005). Patients with a family history of early dissection of the aorta may need more aggressive therapy (Dietz, Cutting et al. 1991). In the latest guidelines for treatment of patients with thoracic aortic disease, it is recommended that a ratio between the maximal cross-sectional area in cm^2 of the ascending aorta or root and the patient's height in meters should be used; if this ratio exceeds 10, surgical repair is reasonable. This is because shorter patients have dissection at a smaller aortic size, and 15% of patients with Marfan syndrome have dissection at an aortic diameter less than 5.0 cm (Hiratzka, Bakris et al. 2010).

β-adrenergic blockers have been used to slow the heart rate, decrease contractility and control arrhythmias, while angiotensin-converting-enzyme (ACE) inhibitors and angiotensin II receptor antagonists have been used for decreasing blood pressure without slowing the heart rate (Canadas, Vilacosta et al. 2010, Matt and Eckstein 2011). The use of β-adrenergic blockade is to reduce the impulse of left ventricular ejection and the heart rate, and thus reduce hemodynamic stress on the proximal aorta in Marfan syndrome (Salim, Alpert et al. 1994, Shores, Berger et al. 1994). There was a trend towards lower mortality, less preventive surgery for aortic dilatation, and fewer cases of dissection after the treatment with β-adrenergic blocker (Ladouceur, Fermanian et al. 2007).

Losartan is an angiotensin II type 1 receptor blocker (ARBs), and was found to be potentially useful in MFS inreducing aortic dilatation (Chiu, Wu et al. 2013, Groenink, den Hartog et al. 2013). The mechanisms explaining the role of losartan are still poorly understood although it is thought to decrease TGF-β1 signaling and activation by reducing the expression of thrombospondin-1 (Tsp-1) (Cohn, van Erp et al. 2007). Tsp-1 is produced by the activation of the angiotensin II type 1 receptor (AT1) by angiotensin (AT), can regulate latent TGF-β1 activation. Hence, losartan can block TGF-β1 activation by inhibiting Tsp-1 production and slow or halt the formation of aortic aneurysms in Marfan patients (Zhou, Poczatek et al. 2006, Chamberlain 2007).

1.2.4. Marfan Mouse Model

A well-established transgenic mouse carrying a single copy of a mutant fibrillin-1 (C1039G) was used for this project (courtesy of H. Dietz at Johns Hopkins University) (Judge, Biery et al. 2004). This mutation was selected to introduce a KpnI restriction site which is useful for genotyping, and substitution of the corresponding cysteine residue in humans (C1039Y) has been associated with classic MFS (Fig. 1.2) (Judge, Biery et al. 2004).

The Cre-Lox recombination technique was used for proper homologous recombination of the endogenous *Fbn1* allele with the targeting vector for the C1039G mutation (Fig. 1.2) (Judge, Biery et al. 2004). Mice with C1039G homozygous mutation uniformly die from vascular catastrophe in the perinatal period (Judge, Biery et al. 2004). Thus, C1039G heterozygous mice were chosen to be the MFS model for this thesis.

Marfan mice have been found to develop many of the classic manifestations of Marfan syndrome, including proximal aortic aneurysms, mitral valve prolapse, pulmonary alveolar septation defects, mild thoracic kyphosis, and skeletal myopathy (Judge, Biery et al. 2004, Habashi, Judge et al. 2006, Gould, Sinha et al. 2012). This mouse model with reduced levels of normal fibrillin-1 replicates many of the features of the Marfan syndrome disease and promises to provide insights into the pathogenesis of the disease (Judge, Biery et al. 2004, Habashi, Judge et al. 2006, Matt, Schoenhoff et al. 2009).

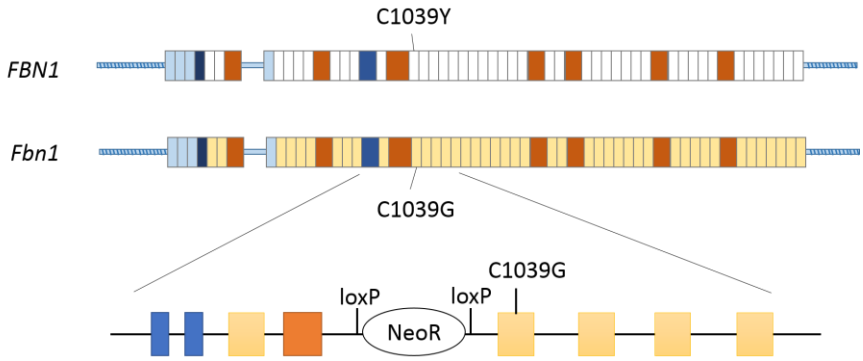

Figure 1.2. Human Human *FBN1* alleles with Mice *Fbn1* alleles and Cre-Lox recombination technique.

The Marfan mouse alleles (*Fbn1*) are shown with full-length human *FBN*1 harboring a mutation that results in classic MFS in humans (C1039Y). The lower panel shows the homologous recombination of *Fbn1* allele with the targeting vector for the C1039G mutation. Mice with this genomic segment will later cross with a CMV-cre mouse to remove the NeoR flanked by loxP sequences. The cbEGF-like domains are shown in yellow (mouse) or white (human); 8-cys LTBP-binding domains are shown in red, and hybrid domains are shown in blue. Figure is modified from (Judge, Biery et al. 2004).

1.3. Echocardiography

1.3.1. Principles of Ultrasound

Echocardiography is the principal tool for non-invasive real-time imaging of the cardiovascular system using ultrasound. Ultrasound technology uses high-frequency sound well above the range of human hearing (20 to ~20,000 Hz). Sound waves have characteristics including frequency (*f*, the number of cycles per unit time), amplitude (the magnitude of waves), wavelength (λ) and the propagation velocity (*c*, the speed that the wave travels through a specific medium) (Solomon and Bulwer 2007). The relationship between propagation velocity, frequency and wavelength is:

$$c = f \times \lambda$$

Typically frequencies of 2-10 MHz are used in diagnostic cardiac ultrasound for humans, and the propagation velocity of sound through water and body tissue is about 1540 m/s (Solomon and Bulwer 2007). Therefore, with a frequency of 5 MHz, the wavelength of ultrasound is about 0.31 mm. As a rule of thumb, the resolution of ultrasound image is about half that of the wavelength. Therefore in this case, a 5 MHz

ultrasound signal has a resolution of approximately 0.15 mm or 150 μm. Based on the same propagation velocity, ultrasound using a higher frequency (i.e. shorter wavelength), yields higher resolution but lower tissue penetrance (Solomon and Bulwer 2007). In our study, the ultrasound frequency was 40-70 MHz which was specifically designed for use with small animals which yields very high resolution (10-20 μm) but low penetration.

Ultrasound can be produced by high-frequency sound beams penetrating the thoracic cavity and reflecting back to the ultrasound transducer when reaching an interface between tissues of different acoustic impedance such as the myocardium, valves, and blood (Gao, Ho et al. 2011). The transit time (depth) and the amplitude (brightness) of the reflected waves are detected by the probe of the ultrasound instrument to generate the image of the reflecting structure within the body (Nihoyannopoulos and Kisslo 2009). For example, the myocardium reflects more of the ultrasound signal so that it appears relatively white compared to blood which reflects little sound and therefore appears relatively black (Nihoyannopoulos and Kisslo 2009).

In addition ultrasound can determine the velocity of moving fluids or tissues by using Doppler mode, which relies on the principle of the Doppler Effect (Taylor and Holland 1990). The Doppler Effect principle is the change in frequency between the emitted and the observed sound wave, which occurs due to the relative motion between the observer and the source (Taylor and Holland 1990). In classical physics, the relationship between observed and emitted frequency is given by:

$$f' = \left(\frac{C + Vr}{C + Vs}\right) f_0$$

Where f' is the observed frequency, f_0 is the emitted frequency from the transducer, *C* is the propagation velocity of sound through the medium (body tissue), Vr is the velocity of the receiver (blood flow) and Vs is the velocity of the source (transducer, Vs = 0). From this Doppler shift equation, the velocity of blood flow can be measured by:

$$Vr = \frac{C(f'' - f_0)}{2f_0 \cos\theta}$$

Where f'' is the returned frequency from the receiver and θ is the angle between the direction of the ultrasound wave propagation and blood flow. If the direction of emitted ultrasound wave is parallel to blood movement, then $\cos 0° = 1$. In contrast, if the direction of emitted ultrasound wave is vertical to blood, then $\cos 90° = 0$, and thus the velocity of blood flow cannot be detected from the echo system in its current configuration.

1.3.2. Introduction of Imaging Views

Bright (B) -mode imaging which displays two-dimensional (2-D) views is the most basic mode of echocardiography and simply produces a real-time black and white image of the heart, valves and major blood vessels (Ram, Mickelsen et al. 2011). It allows a regular distribution of lateral resolution over the entire field and serves, among other things, as a guidance platform to the operator for the correct positioning of various structures for other imaging formats such as M-mode and Doppler-mode imaging (Solomon and Bulwer 2007).

Motion (M) -mode imaging is a one-dimensional (1-D) view that is obtained by a rapid sequence of B-mode scans along a single line and displayed over time. This mode enables precise measurements by providing a very high temporal resolution (e.g. up to 1,000 frames/s or 1 ms temporal resolution on the Vevo 2100 instrument used in the present study) along a narrow ultrasound beam focused on the myocardium (Ram, Mickelsen et al. 2011). Not only can this mode provide images with high temporal and spatial resolution, but it also correlates them with a simultaneously recorded electrocardiogram (ECG) (Solomon and Bulwer 2007). Therefore, global LV functional and anatomical parameters can be obtained from the M-mode short-axis view with high resolution LV contractile tracing of the wall motion between systole and diastole.

Doppler-mode images can be used to determine blood flow velocity and direction (Nihoyannopoulos and Kisslo 2009). Doppler-mode includes color Doppler-mode, continuous wave (CW) and pulsed-wave (PW) Doppler-mode. Color Doppler-mode depicts blood flow direction and velocity superimposed on B-mode images. Red indicates the blood flow moving toward the transducer, while the blue indicates that flow

is moving away from the transducer. Turbulent flow and flow in which the velocities are faster than the limit are seen as a multi-color mosaic signal (Solomon and Bulwer 2007).

In PW Doppler-mode individual pulses of sound waves are emitted to detect the moving sample and the reflected waves then return to the transducer. The rate at which these pulses are emitted is called the pulse repetition frequency (PRF), which is the number of pulses per unit time. PRF is determined by the interrogated depth and the velocity of ultrasound, and it allows the transducer to detect the reflected sound wave before emitting another pulse (Solomon and Bulwer 2007).

In PW Doppler-mode, the depth and position of the sample volume can be controlled, but measuring the velocity of the sample has limitations determined by the Nyquist theorem. Thus if the frequency of the Doppler shift (returned frequency – emitted frequency) is greater than twice the PRF, the velocity cannot be accurately assessed. The PW Doppler mode is used for detecting the blood velocity from a single location, as the sample volume. The X-axis represents time and Y-axis represents the blood flow velocity. By convention, blood flowing towards the probe are plotted above the baseline and blood flowing away from the probe or reverse flow are plotted below the baseline (Nihoyannopoulos and Kisslo 2009). The flow is displayed as a parabolic pattern in this mode because all the red blood cells are not travelling with the same velocity. Laminar blood flow generates the pattern with a big hollow in the middle, suggesting that most of the blood cells are travelling with a similar velocity (Fig. 1.3). On the other hand, turbulent blood flow appears as a filled-in pattern because of the wider range of blood velocities under these conditions (Solomon and Bulwer 2007).

CW Doppler-mode transmits and receives ultrasound waves from the transducer continuously instead of in pulses. The advantage of this mode is that a target with a high velocity can be analyzed since there is no Nyquist limit (Nihoyannopoulos and Kisslo 2009). However, the disadvantage is that a particular position and the depth of the imaging cannot be changed. The region of the sample volume is determined by the overlap of transmitting and receiving ultrasound beams (Nihoyannopoulos and Kisslo 2009). Since the position and the depth of the sample volume were required to be changed throughout the measurement, CW mode was not used in the study.

In addition to the aforementioned attributes of ultrasound that impact imaging, the quality of images is also highly dependent on the operator's skill as well as the position of the transducer and the animal. The specific angle and direction between the transducer and the animal is required for maintaining the consistency of the imaging plane (Solomon and Bulwer 2007). It should also be noted that sound waves do not easily pass through bone and air, ribs and lung can cause significant artifacts to the cardiac imaging. As a consequence reverberation artifacts which are caused by reflections that occur internally can lead to multiple reflection shadows as one probes more deeply into the tissue (Solomon and Bulwer 2007). Other sources of imaging artifacts result from the fact that ultrasound beams can become wider than the scan line and contributes therefore to a loss in lateral resolution (Solomon and Bulwer 2007). These artifacts can affect the quality of echocardiography and make the evaluation challenging.

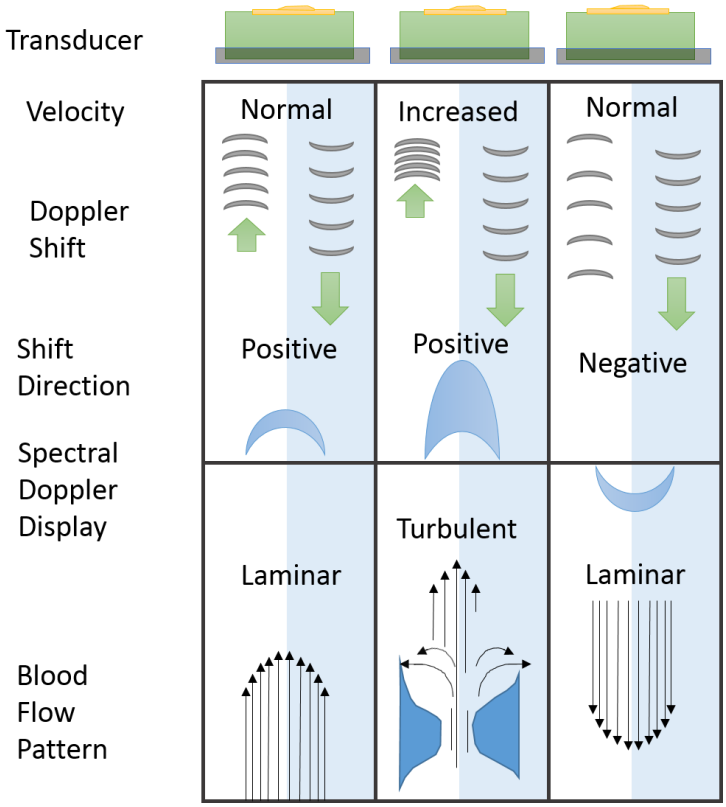

Figure 1.3. The Pulse wave Doppler images displayed of laminar and turbulent blood flow.

Blood flow towards the transducer is displayed in a positive parabolic pattern, while blood flow away from the transducer is presented in a negative parabolic pattern. Figure is modified from (Solomon and Bulwer 2007).

1.3.3. Relevant Equations used in Echocardiography

The LV functional parameters were calculated from the LV short-axis M-mode view. All M-mode measurements should follow the guidelines of the American Society of Echocardiography. Fractional shortening (FS), which is considered as an important parameter for the evaluation of systolic function, can be easily obtained from the following equation (Stypmann, Engelen et al. 2009):

$$\mathrm{FS}(\%) = \left(\frac{LVID;d - LVID;s}{LVID;d}\right) \times 100$$

Where the LVID;d = Average LV end diastolic internal diameter, and LVID;s = Average LV end systolic internal diameter. The FS of an anaesthetized mouse above 30% is considered to be normal.

The LV volume was calculated according to the Teichholz equation (Stypmann, Engelen et al. 2009):

$$\mathrm{ESV}\ (\mu\mathrm{l}) = \frac{7 \times (LVID;s)^3}{[2.4 + LVID;s]}$$

$$\mathrm{EDV}\ (\mu\mathrm{l}) = \frac{7 \times (LVID;d)^3}{[2.4 + LVID;d]}$$

Where the ESV = End systolic volume, and EDV = End diastolic volume. From these two values, other functional parameters such as stroke volume (SV), cardiac output (CO), ejection fraction (EF) can be acquired by using following equations:

$$\text{Stroke volume}\ (\mu\mathrm{l}) = EDV - ESV$$

$$\text{Cardiac output}\ (\mathrm{ml/min}) = \frac{SV \times HR}{1000}$$

$$\text{Ejection fraction}\ (\%) = 100 \times \frac{EDV - ESV}{EDV}$$

For the mass of the LV myocardium, there are several different algorithms one can use. The algorithm used in this thesis is derived from the Penn convention and is also based on the short-axis M-mode view (Devereux and Reichek 1977):

$$\text{LV mass (mg)} = 1.05 \times [(LVAW;d + LVID;d + LVPW;d)^3 - (LVID;d)^3]$$

$$\text{LV mass (Corrected)} = \text{LV mass} \times 0.8$$

Where the LVAW;d = Average LV end diastolic anterior wall thickness, and LVPW;d = Average LV end diastolic posterior wall thickness. The factor 1.05 represents the specific gravity of myocardial tissue.

In the clinic, the cardiac structural parameters derived from echocardiography such as LV volume, mass, wall thickness are usually normalized with respect to the patients' body surface area (BSA). For example, the cardiac index (CI), which is equal to cardiac output (CO) divided by BSA, is widely used in ultrasound diagnosis for human patients.

Mouse BSA can be estimated from body mass with a constant k, which is determined by species and size (k for C57BL/6J mice is 9.82). Animal BSA is calculated from the following equation (Cheung, Spalding et al. 2009) :

$$\text{BSA}(\text{cm}^2) = \text{k} \times \text{mass}^{0.667}(\text{g})$$

In this study, the weight of Marfan mice was generally lighter than WT in both the six- and twelve-month groups although it did not reach a statistically significant level. Besides, the mice in between six- and twelve-month groups were not the same subjects. Therefore, in order to reduce individual difference of mice, we simply normalized certain body size-dependent cardiac structure parameters which include: EDV, ESV, SV, CO, LV mass, LVAW, IVS and LVPW by mouse body weight.

The limitation of M-mode functional measurements is that these parameters are estimated by assuming symmetry of the LV; besides cardiac function is only assessed at the one dimensional level, unlike measurements in B-mode view which are assessed

based on the area of LV at two dimensional levels (Stypmann, Engelen et al. 2009). Therefore, M-mode measurements are not applicable for models with asymmetrical LV (e.g. acute or chronic myocardial injury models), since the equations are under the premise of a symmetric LV model (Stypmann, Engelen et al. 2009).

However, the M-mode measurement was still used in our study because it provides a very high temporal resolution (up to 1,000 frames/s) of tissue motion. It allows one to create a very precise tracing along the epicardial and endocardial wall borders. Furthermore, this mode is able to correlate with a simultaneously recorded electrocardiogram (ECG). Therefore, M-mode measurement is easier to acquire and more reliable than the B-mode measurements, and consequently reducing human error.

Chapter 2. Materials and Methods

2.1. Animals

Six- and twelve-month old Marfan [*Fbn1* (C1039G/+)] mice (courtesy of H. Dietz at Johns Hopkins University) and wild-type (WT) littermates (*Fbn1* +/+) were studied. Marfan mice were mated with WT mice to generate *Fbn1* (C1039G/+) and *Fbn1* +/+ littermates for experimental and control groups, respectively. Animals were housed in the animal facility of the Child and Family Research Institute (CFRI), University of British Columbia (UBC) with standard animal room conditions (25°C, 12-hour light-dark, <5 animals in a cage). All experiment procedures were approved by the UBC animal ethics board.

2.2. Animal Preparation

Anesthesia was induced by putting the mouse in an induction chamber using 3% isoflurane and 1 L/min 100% oxygen for 1-2 minutes. Once the animal lost its righting reflex, it was laid supine on a heated platform with its nose enveloped in a nosecone to keep the mouse anesthetized by1.5-2% isoflurane (Roth, Swaney et al. 2002, Gao, Ho et al. 2011). The mouse limbs were taped to four ECG electrodes which were imbedded in the platform for heart rate, ECG and respiratory rate monitoring. One drop of eye lubricant (Tears Naturale®, Hünenberg, Switzerland) was applied on each eye to prevent corneal drying and damage. Body temperature was monitored through a rectal probe, and maintained at 36-38℃ with a heating lamp and the heated platform. Chest hair was removed with a hair remover (Nair© Church & Dwight Co.) and 5 ml of Ultrasound gel (Aquasonic Clear®, Fairfield, NJ, USA) was applied on the chest before imaging for better sound wave conduction between skin and transducer.

Isoflurane is the most commonly used inhalational anesthetic for experimental animals to remain in the appropriate anesthetized stage for a relatively long period of time, and it has been widely used for animal imaging technologies (Constantinides, Mean et al. 2011). Despite the fact that isoflurane can depress cardiac function, it has some advantages including easier control of the animal anesthetic level and faster induction and recovery compared with other inhalational anesthetics (Ludders 1992). 1.5% isoflurane was considered to be the most appropriate dose level with stable mean arterial pressure and heart rate which were comparable to those observed in the conscious mice (Constantinides, Mean et al. 2011).

Heart rate is one of the crucial criteria for the echo imaging recording. The higher heart rate (475–525 bpm) in mice has been shown to be commensurate with increased EF, FS and LV mass compared with lower heart rate groups (350-400 bpm) (Wu, Bu et al. 2010). Maintaining higher heart rate (475–525 bpm) under isoflurane anesthesia has been suggested to result in more reproducible echocardiographic measurements. The echocardiographic results of mice showed no significant difference between short isoflurane anesthetic timing (5.0 ± 2.5 minutes, 2%) and long isoflurane anesthetic timing (10.0 ± 2.5 min, 2%) group (Wu, Bu et al. 2010).

Therefore, mice with heart rates below 400 bpm or ejection fractions under 45% were rejected from our data collection. If the heart rate was not in our required range, it could be adjusted by temporarily increasing (3-5%) or decreasing (0.5-1%) the isoflurane concentration to decrease or increase heart rate, respectively. Once the heart rate reached our criterion range, the isoflurane concentration was changed back to the normal 1.5-2%.

2.3. Image Acquisitions and Analysis

A Vevo 2100 ultrasound system (VisualSonics®, Toronto, ON, Canada) equipped with a MS550 transducer was used for the mouse echocardiography. The transducer has a central frequency of 40 MHz, a focal length of 7.0 mm, and a frame rate of 557 fps (single zone, 5.08 mm width, B-mode). The maximum field of view of 2D imaging was 14.1 x 15.0 mm with a spatial resolution of 90 µm (lateral) by 40 µm (axial).

All the measurements were produced using the VisualSonics' cardiac-package software and each parameter measurement was repeated over five cardiac cycles to reduce bias. All image acquisitions and the analysis were conducted by a single investigator who was blinded as to animal groups. Data were collected from four different views as described below.

2.3.1. Parasternal long-axis view

To perform the long-axis view, the heated platform was angled head-up and rotated leftward for a 15° deviation from the coronal plane. The transducer was tilted 70° from the coronal plane and rotated approximately 35° counter-clockwise (Fig. 2.1) (Zhou, Foster et al. 2004). Left ventricle, left atrium, aortic outflow tract and part of right ventricle were visualized in this view (Zhou, Foster et al. 2004). M-mode was recorded from the tip of the papillary muscle in the left ventricle for measuring the interventricular septal and posterior wall thickness (Ram, Mickelsen et al. 2011).

Pulmonary artery flow could be assessed from the Doppler-mode with the transducer slightly shifted to the right on the x-axis. Peak velocity and velocity time integral(VTI) were calculated from these data (Ram, Mickelsen et al. 2011).

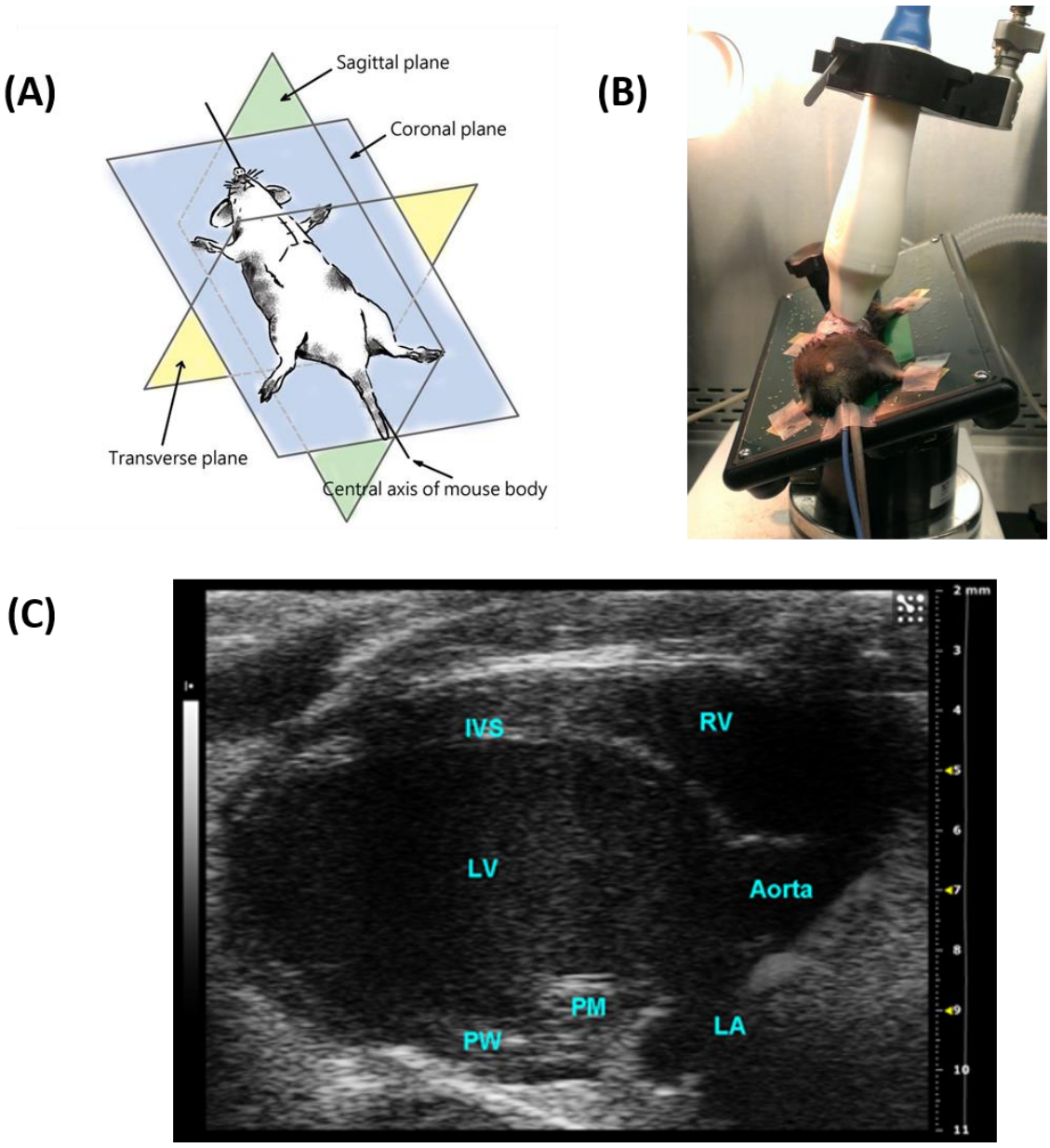

Figure 2.1. Long-axis view of a mouse left ventricle.
(A) The three orthogonal planes of the mouse body. Picture is modified from (Zhou, Foster et al. 2004). **(B)** The orientation of the echo transducer and the platform for long-axis view. **(C)** The B-mode image of long-axis view. IVS, interventricular septum; LA, left atrium; LV, left ventricle; PM, papillary muscle; PW, posterior wall; RV, right ventricle.

2.3.2. Parasternal short-axis view

Once the imaging of the long-axis views was completed, the transducer was rotated 90° counter-clockwise for obtaining the parasternal short axis view (Fig. 2.2 A) (Zhou, Foster et al. 2004). The transducer had to be adjusted until the two papillary muscles appeared at the two and five o'clock positions (Ram, Mickelsen et al. 2011). Left and right ventricles were visualized in this view. An M-mode cursor was positioned perpendicular to the anterior and posterior walls, in the middle of the LV for measuring wall thickness and chamber dimensions (Fig. 2.2 C). Left ventricular functional parameters (stroke volume, ejection fraction, fractional shorting and cardiac output) and structural parameters (LV mass, anterior and posterior wall thickness) were obtained from this M-mode, which was recorded in the middle of the left ventricle (Gao, Ho et al. 2011).

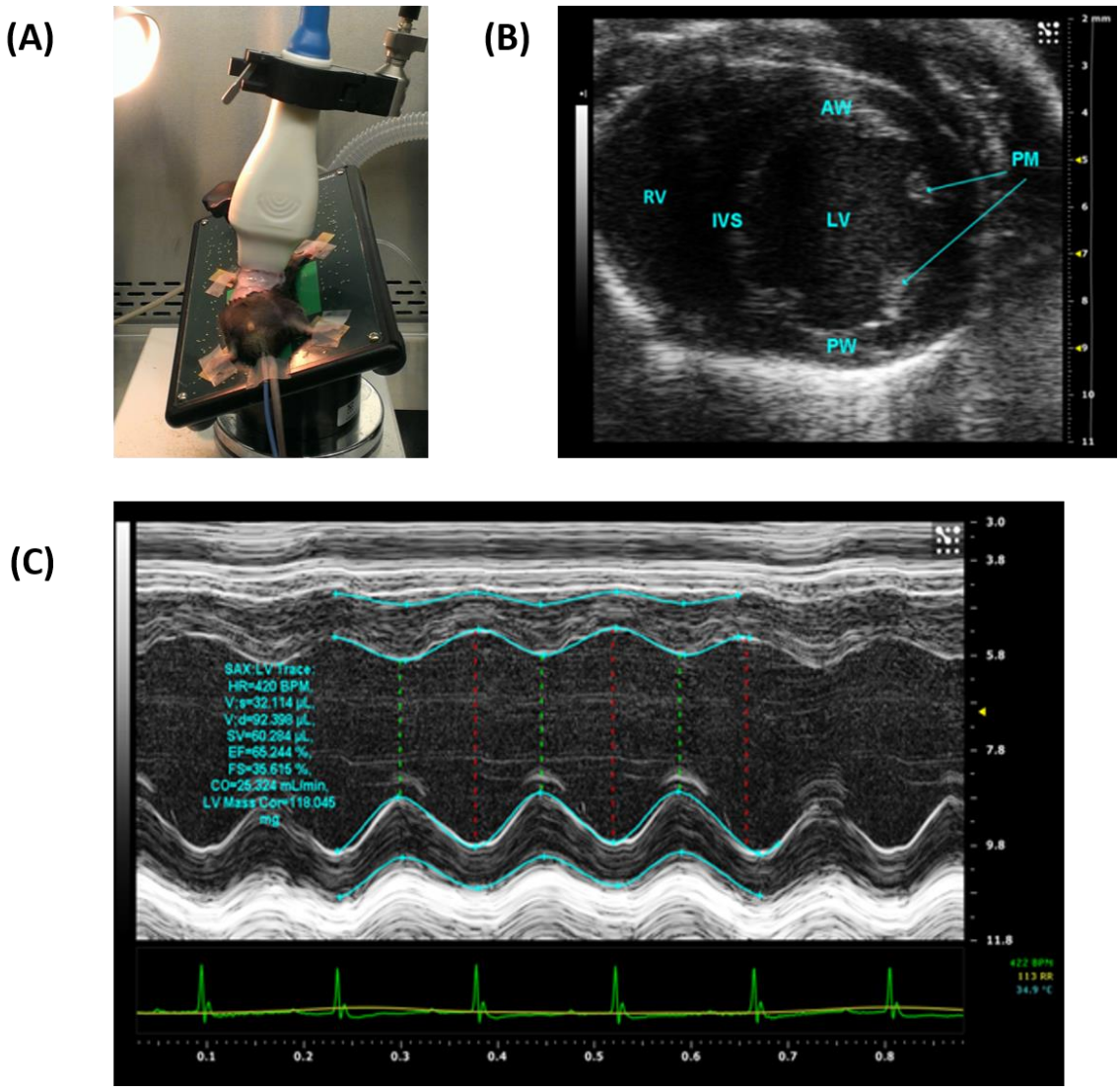

Figure 2.2. Short-axis view of a mouse left ventricle.
(A) The orientation of the echo transducer and the platform for short-axis view. **(B)** B-mode image of short-axis view. **(C)** M-mode images show the LVAW, LV chamber and LVPW throughout diastole (d) and systole (s). Tracing of the wall along the epicardial and endocardial borders allows an assessment of cardiac functional parameters. IVS, interventricular septum; AW, anterior wall; LV, left ventricle; PM, papillary muscle; PW, posterior wall; RV, right ventricle; HR, heart rate; SV, stroke volume; EF, ejection fraction; FS, fractional shortening; CO, cardiac output.

2.3.3. Aortic arch view

In this view, the entire aortic arch and its three branches (IA, innominate artery; LCCA, left common carotid artery; LSA, left subclavian artery) were well visualized in a right parasternal longitudinal section (Fig. 2.3) (Ram, Mickelsen et al. 2011). The platform was 40° clockwise rotated with the coronal plane and the transducer was tilted

toward the right with about a 70° deviation with the coronal plane (Zhou, Foster et al. 2004). Aortic diameters (aortic annulus (L1), sinuses of valsalva (L2) and sinotubular junctions (L3)) were measured from the B-mode (Fig. 2.3 B). The ascending and descending aortic peak velocity and the velocity time integral (VTI) could be measured from the PW Doppler-mode.

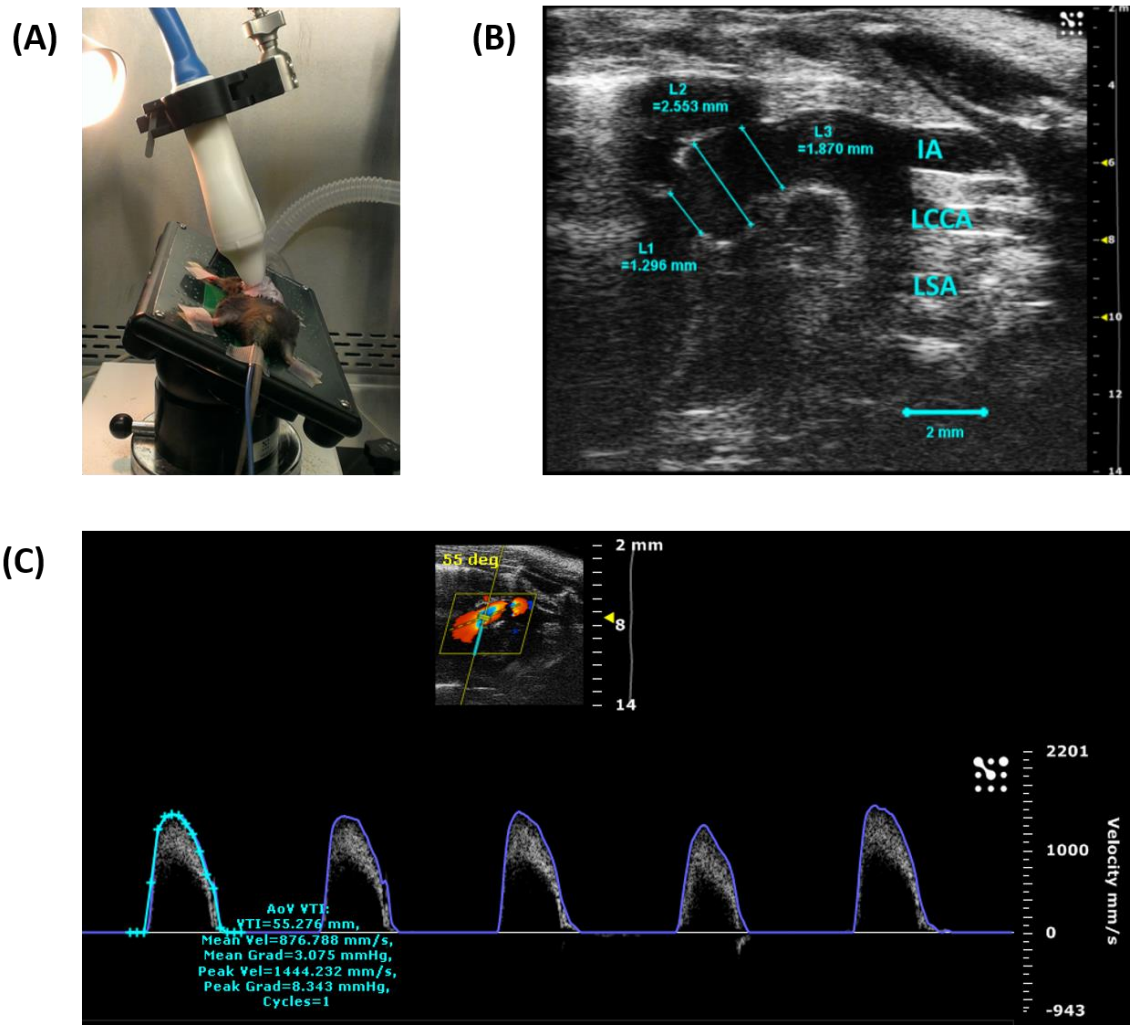

Figure 2.3. B-mode and Doppler-mode image views of a mouse aortic arch.
(A) The orientation of the echo transducer and the platform for the aortic arch view. **(B)** B-mode view of the aortic arch from a 6-month Marfan mouse. Diameters of the aortic annulus (L1), sinus of valsava (L2) and sinotubular junction (L3) were indicated by cyan lines. Scale bars, 2 mm. **(C)** Color Doppler (upper panel) and Pulsed-wave Doppler (lower panel) imaging of the ascending aorta. Sample volume was placed in the middle of aortic root (upper panel) to generate the flow velocity profile (lower panel). The peak velocity and VTI of the blood flow could be obtained by tracing the border of a wave (cyan line). The Y-axis indicates velocity (mm/s) and the x-axis indicates time (ms). IA, innominate artery; LCCA, left common carotid artery; LSA, left subclavian artery; velocity time integral (VTI).

2.3.4. Apical four chamber view

To access this view, the platform was angled head-down and rotated leftward for 45° with coronal plane (Zhou, Foster et al. 2004). The transducer was tilted toward the apex of the heart about 70° with coronal plane. The left and right ventricles were visualized in this view as well as the two atria were clearly visible at the bottom of the screen (Fig. 2.4) (Ram, Mickelsen et al. 2011). The mitral flow velocity which includes both E and A waves were acquired from the Doppler-mode when the sample volume placed directly under the mitral valves (Fig. 2.4 B). The isovolumic contraction time (IVCT), isovolumic relaxation time (IVRT) and ejection time (ET) could also be measured under this view (Ram, Mickelsen et al. 2011). The myocardial performance index (MPI), which was calculated by (IVCT + IVRT)/ ET, could be calculated for evaluating the LV systolic and diastolic function (Arnlov, Ingelsson et al. 2004).

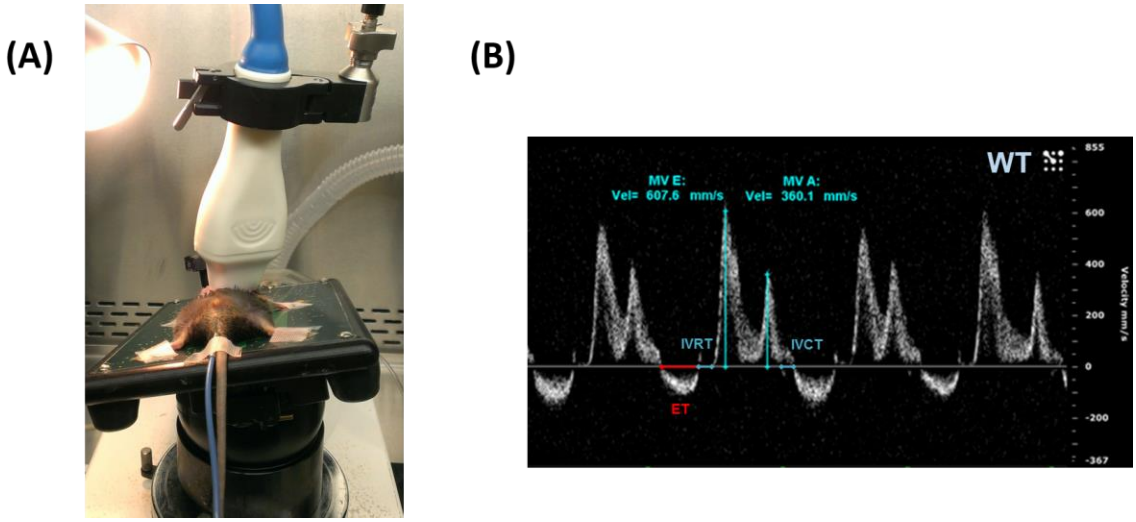

Figure 2.4. The apical four chamber view of a WT mouse.
(A) The orientation of the echo transducer and the platform for apical four chamber view. **(B)** The mitral inflow velocity profiles of WT mice were obtained within the mitral valve region shown from the apical four-chamber view. The velocity (in mm/s, y-axis) is shown over time (in ms, x-axis). Inset: early filling peak velocity (MV E) during LV relaxation, and the atrial filling peak velocity (MV A) during atrial contraction. IVCT, isovolumic contraction time; IVRT, isovolumic relaxation time; ET, Ejection time (indicated by red arrow).

2.4. Pulse Wave Velocity Analysis

Pulse-wave velocity (PWV) was obtained from the B-mode and Doppler-mode aortic arch view, and the calculation used was PWV = aortic arch distance / transit time

(cm/s) (Fig. 2.5) (Hirata, Triposkiadis et al. 1991). PW Doppler Mode sample volume was placed in the ascending aorta and the time (T1) from the onset of the QRS complex to the onset of the ascending aortic Doppler waveform was measured (Bradley, Potts et al. 2005).

On the same image plane, PW Doppler Mode sample volume was placed as distal as possible in the descending aorta and the time (T2) from the onset of the QRS complex to the onset of the ascending aortic Doppler waveform was measured (Bradley, Potts et al. 2005). T1 and T2 were averaged over 10 cardiac cycles. The aortic arch distance was measured between the 2 sample volume positions along the central axis of aortic arch on the B-mode image, and the transit time was calculated by T2 – T1 (ms) (Bradley, Potts et al. 2005).

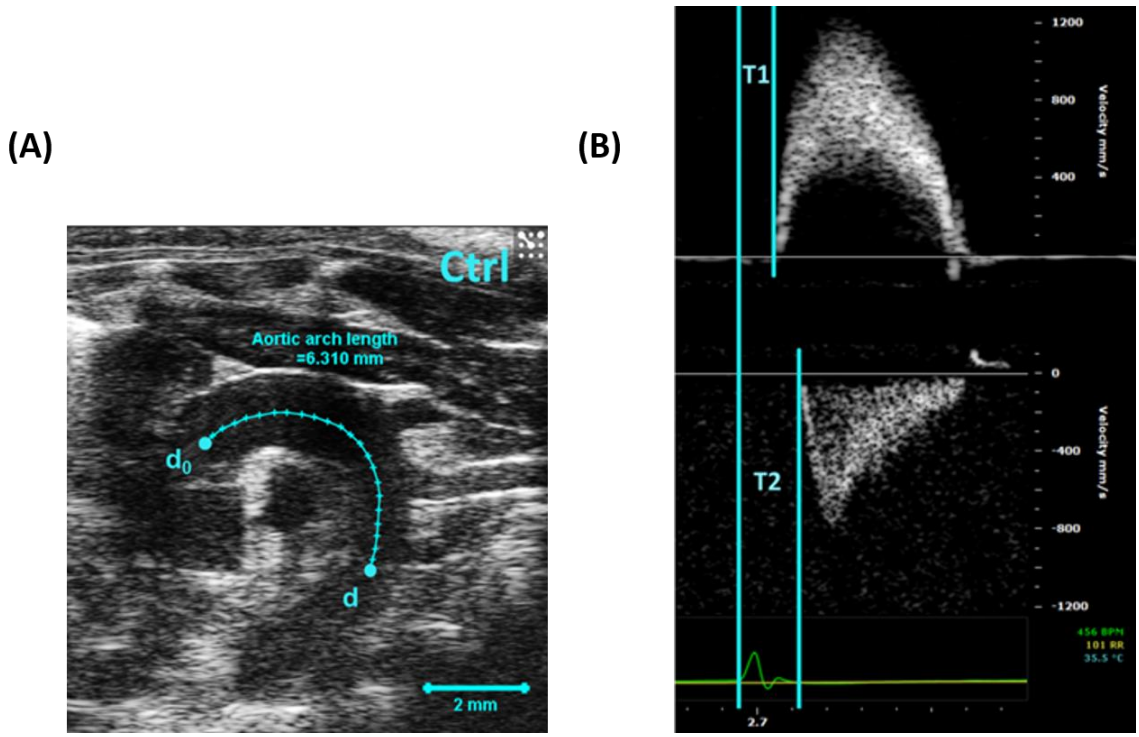

Figure 2.5. Pulse wave (PW) velocity of aortic arch.
(A) B-mode view of the aortic arch of a 6-month wild type (WT) mouse. The distance between ascending and descending aorta pulse wave Doppler recordings was indicated by the cyan-colored line (d0 to d). **(B)** Pulse wave Doppler tracing of the ascending (upper panel) and descending aorta (lower panel). X-axis represents time (ms) and Y-axis represents blood flow velocity (mm/s). T1 was measured from the beginning of the QRS wave on the ECG to the beginning of the ascending aortic peak velocity and T2 was the beginning of the QRS wave on the ECG to the beginning of the descending aortic peak velocity. Pulse wave velocity was calculated using the distance between d0 and d in the aortic arch divided by the transit time (i.e. [d-d0] / [T2-T1]).

2.5. Strain Analysis

Strain analysis is a modified echocardiographic technique that uses speckle-tracking applied on high-frequency ultrasound images for the evaluation of both regional and global left ventricular (LV) function (Bauer, Cheng et al. 2011). The speckles are visible in the B-mode images and are equally distributed within the myocardium. The speckles can be tracked consecutively frame to frame to quantitate the motion of tissues in the heart. Strain represents deformation of the heart, which was defined as the change in the length of a segment divided by its original length ([L1-L0]/L0). Strain rate (SR) was the change of this deformation per unit time ([(L1-L0)/L0] x sec-1) (Bauer, Cheng et al. 2011).

The speckle-tracking based strain analysis was applied on parasternal long- and short-axis B-mode views, and the myocardial motion was quantified into three axes: longitudinal, radial, and circumferential axes (Fig. 2.6 B) (Ram, Mickelsen et al. 2011). Longitudinal and circumferential strain showed negative curves because it represents shortening of the myocardium, whereas radial strain demonstrated a positive curve because it represents lengthening of the myocardium. Parasternal long-axis views provided longitudinal and radial strain, and parasternal short-axis views were obtained for circumferential and radial strain analyses (Fig. 2.6) (Ram, Mickelsen et al. 2011).

A B-mode image was acquired with a frame rate at least 200 fps, and with adequate visualization of the LV endocardial and epicardial border. Data analysis was performed using a speckle-tracking algorithm provided by VisualSonics (VevoStrain, VisualSonics) with semiautomated tracing of the endocardial and epicardial borders over two cardiac cycles. The tracing was corrected on each frame. The left ventricle was divided into six segments for regional strain analysis on both long- and short-axes. The strain measures were averaged over the selected cardiac cycle and displayed into 6 curves (Fig. 2.6). On each segment, peak strain and SR measurements were recorded, and the global peak strain and SR measurements were the average of the 6 segments' values.

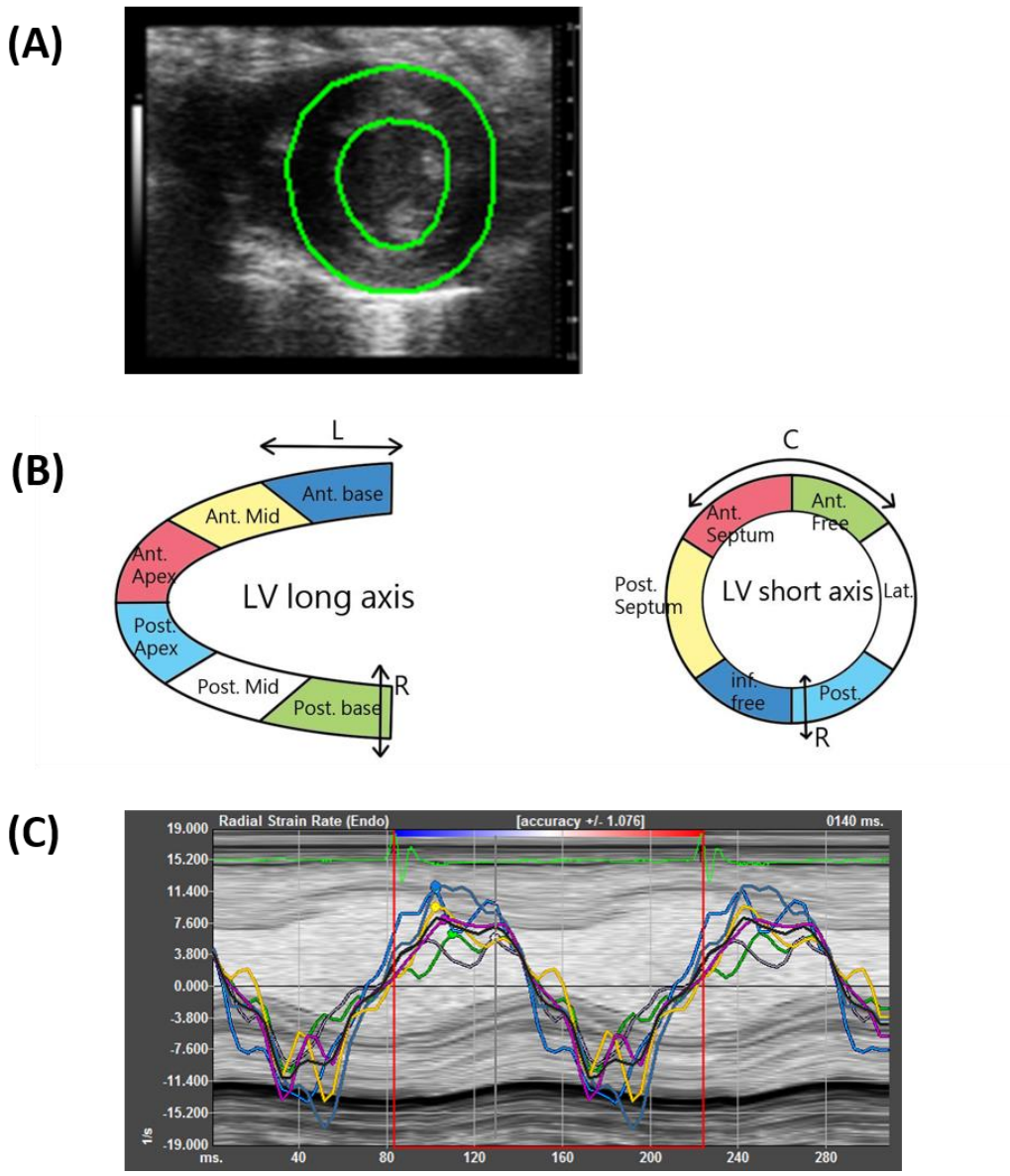

Figure 2.6. Strain rate of WT and MSF mice.

(A) Speckle-tracking based strain analysis from a B-mode short axis image of a 12-month Marfan mouse left ventricle. Endocardial and epicardial borders were indicated by green tracings. **(B)** Three directions of myocardial deformation including longitudinal (L), circumferential (C), and radial (R) axis. The LV wall was divided into six regional segments in both long- (left) and short-axis (right). **(C)** A short-axis regional and global strain rate (1/s) curves were shown, the color of the lines corresponded to the specific segments in panel (B) short-axis image. Red box showed the selected one cardiac cycle. Ant, anterior; Inf, inferior; Lat, lateral; Post, posterior.

2.6. Statistics

A power analysis (JMP version 10) was performed using our preliminary data. To see a biological importance of 0.4 mm sinuses of valsalva dimension difference and of 0.3 mm interventricular septal thickness difference with 80% power, our sample size for the best scenario needed to be at least 8 mice per group. Independent Student's t-test (JMP version 10) was used to determine statistical significance between 6-month WT vs. MFS, 12-month WT vs. MFS and 6-month MFS vs. 12-month MFS groups. A P value less than 0.05 was accepted as statistical significance.

Chapter 3. Results

3.1. Left Ventricular Functional Analysis

The LV ventricular functional data obtained from the LV trace of short-axis M-mode images are displayed in Table 3.1. End systolic volume (ESV), end diastolic volume (EDV), stroke volume (SV) and cardiac output (CO) were normalized with respect to body weight (BW) to avoid individual growth-influenced differences. There were no significant differences in heart rate (HR), BW, ejection fraction (EF) and fractional shortening (FS) between WT and Marfan mice group in both 6 months and 12 months.

The results indicate that the normalized EDV, SV and CO were significantly increased by 21% (p = 0.03), 30% (p = 0.005) and 31% (p = 0.02), respectively in Marfan mice at 6 months, but the difference was not observable in the 12 months group. The data suggest that Marfan mice have dilated left ventricles in the early stage.

Table 3.1. Echocardiographic functional analysis for WT and MFS mice.

Parameters (unit)	6 months group			12 months group			6 vs. 12 m
	WT	MFS	P	WT	MFS	P	MFS *P*
Body weight (g)	39.12 ± 0.98	37.55 ± 1.10	0.31	41.89 ± 1.30	37.22 ± 2.20	0.09	0.90
Heart Rate (bpm)	434.12 ± 21.45	432.1 ± 9.96	0.93	453.26 ± 10.65	462.65 ± 18.25	0.67	0.17
End systolic volume (N) (µl/g)	0.76 ± 0.08	0.81 ± 0.08	0.68	0.78 ± 0.07	0.62 ± 0.11	0.23	0.18
End diastolic volume (N) (µl/g)	1.96 ± 0.09	2.37 ± 0.14	0.03*	1.97 ± 0.09	1.90 ± 0.17	0.73	0.06
Stroke volume (N) (µl/g)	1.20 ± 0.05	1.56 ± 0.09	0.005**	1.20 ± 0.07	1.29 ± 0.13	0.54	0.10
Ejection fraction (%)	61.83 ± 3.16	66.12 ± 2.26	0.29	60.74 ± 2.87	68.16 ± 3.68	0.14	0.64
Fractional shortening (%)	33.27 ± 2.32	36.45 ± 1.66	0.29	32.48 ± 1.99	38.07 ± 2.66	0.12	0.61
Cardiac output (N) (ml/min/g)	0.52 ± 0.03	0.68 ± 0.05	0.02*	0.54 ± 0.03	0.60 ± 0.06	0.45	0.34

All results are presented as Means ± SEM (n = 8 mice). * indicates $p < 0.05$, ** indicates $p < 0.01$. N, normalized with body weight.

The mitral inflow velocity measurements were obtained using PW Doppler imaging within the mitral valve sampling region shown from the apical four-chamber view (Table 3.2). The data showed that isovolumic relaxation time (IVRT) was significantly prolonged in 12 months Marfan mice compared with WT ($p < 0.001$). Ejection time (ET) indicated no difference between Marfan and WT mice at 6- and 12-month, but was significantly decreased in 12 months Marfan group compared with 6 months Marfan group ($p = 0.002$). The myocardial performance index (MPI), which is calculated by (IVCT + IVRT)/ ET, was increased by 36% in 12-month MFS mice ($p < 0.001$) compared with WT and was increased by 28% in 12-month Marfan mice ($p < 0.001$) compared with 6-month Marfan mice (Fig 3.1).

Mitral valve early (E) velocity was decreased significantly by 37% and 46% in Marfan mice compared with WT at 6-month ($p <0.001$) and 12-month old ($p <0.001$), respectively (Fig. 3.1). Mitral valve atrial (A) velocity showed no difference between Marfan and WT mice in 6-month, but was decreased significantly by 24% in Marfan at 12-month ($p = 0.01$). As a consequence, the E/A ratio was significantly decreased in Marfan mice versus WT in both 6-month (36%, $p < 0.001$) and in 12-month (29%, $p < 0.001$) groups, respectively (Fig. 3.1). All these data are consistent with the notion that left ventricular diastolic dysfunction developed in Marfan mice at both 6- and 12-month groups.

Table 3.2. Echocardiographic assessment of mitral valve flow for WT and Marfan mice.

Parameters (unit)	6 months group			12 months group			6 vs. 12
	WT	MFS	P	WT	MFS	P	MFS *P*
IVCT (ms)	17.69 ± 0.96	17.44 ± 0.66	0.83	16.31 ± 1.05	18.46 ± 1.65	0.29	0.58
IVRT (ms)	16.38 ± 0.67	17.73 ± 0.74	0.20	14.52 ± 0.85	20.08 ± 0.98	<0.001***	0.08
ET (ms)	48.75 ± 1.58	47.55 ± 1.08	0.54	43.78 ± 0.91	40.48 ± 1.47	0.08	0.002**
MPI	0.70 ± 0.02	0.74 ± 0.04	0.32	0.70 ± 0.03	0.95 ± 0.03	<0.001***	<0.001***
E velocity (mm/s)	597.30 ± 20.29	373.44 ± 31.10	<0.001***	599.36 ± 18.42	323.11 ± 32.26	<0.001***	0.28
A velocity (mm/s)	364.66 ± 20.31	352.15 ± 26.86	0.72	417.81 ± 21.78	319.37 ± 23.10	0.01**	0.37
E/A ratio	1.67 ± 0.09	1.07 ± 0.06	<0.001***	1.45 ± 0.04	1.02 ± 0.07	<0.001***	0.65

All results are presented as Means ± SEM (n = 8 mice). ** indicates $p < 0.01$, *** indicates $p < 0.001$. IVCT, isovolumic contraction time; IVRT, isovolumic relaxation time; ET, Ejection time; MPI, Myocardial performance index.

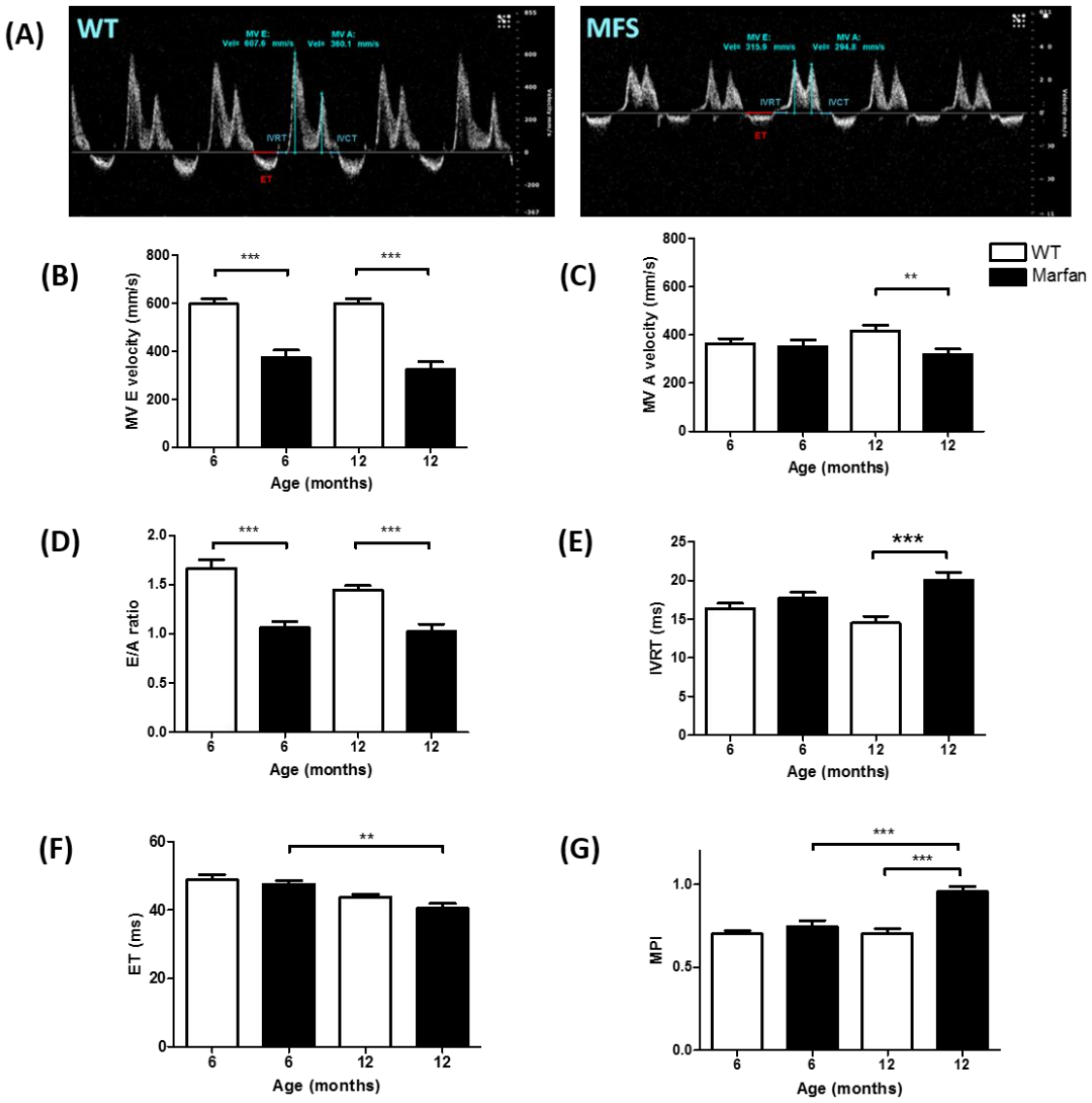

Figure 3.1. Mitral inflow velocity of WT and Marfan mice.
(A) Mitral inflow velocity profile of WT (left panel) and Marfan (right panel) mice at f 6-months. Velocity (mm/s, y-axis) is shown as a function of time (ms, x-axis). Mitral valve early peak (MV E) velocity was determined from the first peak and atrial peak velocity (MV A) from the second peak. Isovolumic relaxation time (IVRT), isovolumic contraction time (IVCT) and ejection time (ET) are displayed in blue and red lines, respectively. **(B)** MV E velocity, **(C)** MV A velocity, **(D)** E/A ratio, **(E)** IVRT, **(F)** ET and **(G)** Myocardial performance index (MPI) from WT and Marfan mice. (n = 8) ** indicates $p < 0.01$, *** indicates $p < 0.001$.

3.2. Left Ventricular and Aortic Structural Analysis

Left ventricle (LV) mass, systolic and diastolic wall thickness were calculated from M-mode of the LV long and short axis view and normalized with respect to body

weight (g) (Table 3.3). Systolic (p = 0.04) and diastolic (p = 0.045) anterior wall thickness were significantly increased by 22% and 32% in Marfan mice compared to WT at 12-month of age, respectively. Systolic (p = 0.02) and diastolic (p = 0.03) posterior wall thickness also increased by 31% and 23% in Marfan mice compared to WT at 12-month of age, and systolic (p = 0.03) posterior wall thickness was increased by 14% in the 6-month group. Systolic (p = 0.02) and diastolic (p = 0.03) interventricular septal thickness were significantly increased in Marfan mice compared to WT at 6-months of age both by 21%. The LV mass which was calculated from these measurements, was significantly increased by 25% in Marfan mice compared to WT at 6-months of age (p = 0.007) (Fig 3.2).

Table 3.3. Echocardiographic LV structural analysis for WT and MFS mice.

Parameters (unit)	6 months group			12 months group			6 vs. 12 m
	WT	MFS	P	WT	MFS	P	MFS *P*
LV mass (N) (mg/g)	2.46 ± 0.09	3.06 ± 0.16	0.007**	2.57 ± 0.05	2.82 ± 0.18	0.22	0.34
Diastolic LVAW (N) (μm/g)	21.78 ± 0.55	24.14 ± 1.14	0.09	20.65 ± 1.10	27.24 ± 2.64	0.046*	0.31
Systolic LVAW (N) (μm/g)	29.64 ± 1.32	32.11 ± 1.52	0.24	28.39 ± 1.25	34.77 ± 2.41	0.04*	0.37
Diastolic LVPW (N) (μm/g)	19.22 ± 0.57	20.34 ± 0.75	0.26	19.12 ± 0.61	23.52 ± 1.59	0.03*	0.10
Systolic LVPW (N) (μm/g)	26.77 ± 1.09	30.50 ± 1.09	0.03*	26.94 ± 1.37	35.29 ± 2.85	0.02*	0.15
Diastolic IVS (N) (μm/g)	20.82 ± 1.01	25.22 ± 1.44	0.03*	21.11 ± 1.62	26.97 ± 2.21	0.05	0.52
Systolic IVS (N) (μm/g)	27.67 ± 1.84	33.39 ± 1.15	0.02*	28.92 ± 1.83	33.71 ± 2.33	0.13	0.90

All results are presented as Means ± SEM (n = 8 mice). * indicates $p < 0.05$, ** indicates $p < 0.01$. AW, anterior wall; IVS, interventricular septum; LV, left ventricle; N, normalized with body weight; PW, posterior wall.

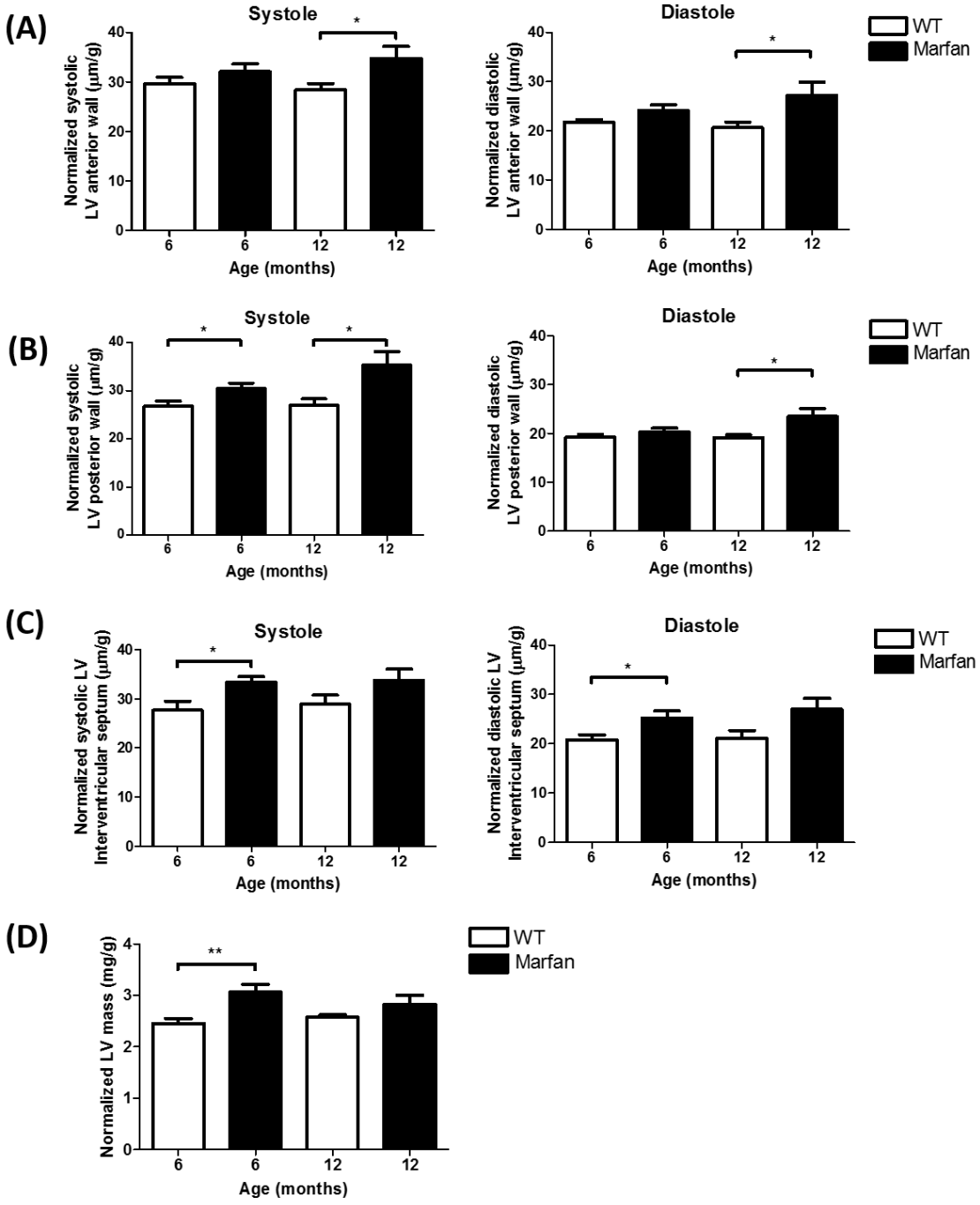

Figure 3.2. Echocardiographic assessment of left ventricle (LV) mass and wall thickness.

Left ventricle (LV) mass, systolic and diastolic wall thickness were calculated from M-mode of the LV long and short axis view, and normalized by body weight (g). Data presented are normalized systolic and diastolic (A) anterior wall thickness, (B) posterior wall thickness, (C) interventricular septal thickness and (D) normalized LV mass from WT and Marfan mice. * indicates $p < 0.05$, ** indicates $p < 0.01$.

For the aortic structure, the diameter of aortic root was obtained from the B-mode view of the aortic arch (Table 3.4). Our results indicate that the aortic annulus diameter was significantly increased by 18% in Marfan mice versus WT in 6-month (p = 0.01) and by 27% in 12-month (p = 0.003) groups, respectively. The diameter of the sinus of Valsava was also significantly increased in Marfan mice versus WT by 19% in 6-month (p < 0.001) and by 27% in 12-month (p = 0.002) groups, respectively. The diameter of the sinotubular junction was increased by 13% in Marfan mice versus WT at 6-month (p = 0.008) of age but the difference in 12 months was not found to be significant (Fig. 3.3). The data clearly illustrate a progressive aortic root dilation in the Marfan mice.

Table 3.4. Echocardiographic analysis of aortic root diameter for WT and MFS mice.

Parameters (unit)	6 months group			12 months group			6 vs. 12
	WT	MFS	*P*	WT	MFS	*P*	MFS *P*
Aortic annulus (mm)	1.33 ± 0.03	1.57 ± 0.07	0.01**	1.38 ± 0.04	1.74 ± 0.09	0.003**	0.14
Sinus of Valsalva (mm)	2.16 ± 0.04	2.56 ± 0.07	<0.001***	2.21 ± 0.07	2.81 ± 0.13	0.002**	0.12
Sinotubular junction (mm)	1.50 ± 0.04	1.70 ± 0.05	0.008**	1.61 ± 0.06	1.75 ± 0.08	0.20	0.60

All results are presented as Means ± SEM (n = 8 mice). ** indicates p < 0.01.

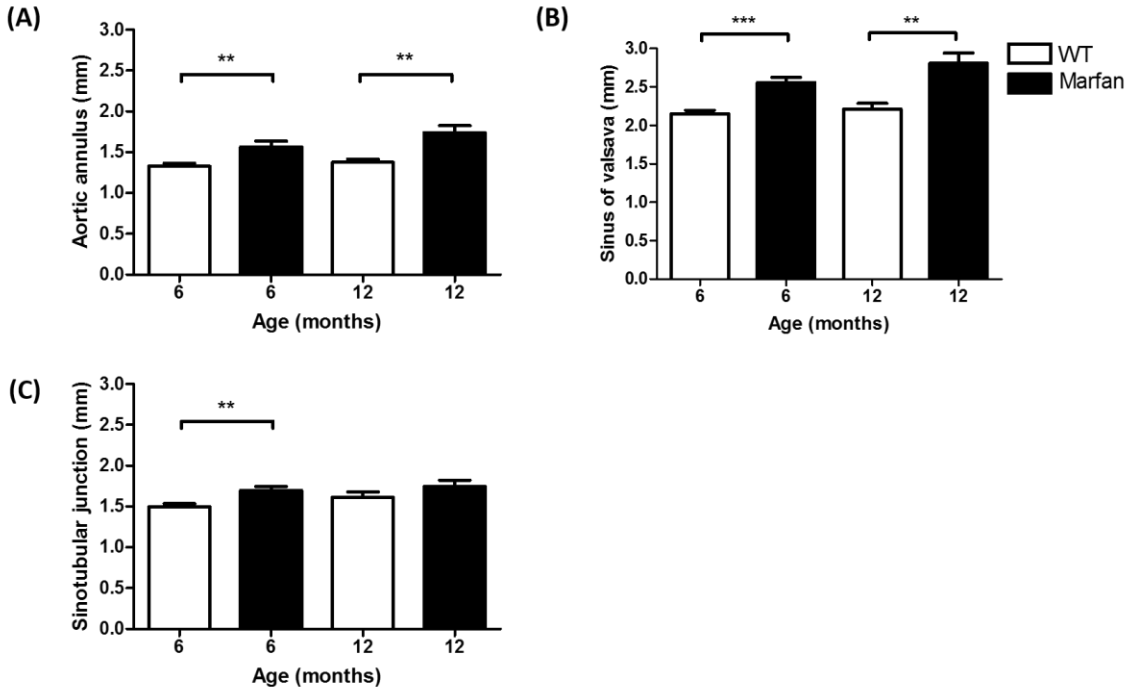

Figure 3.3. Aortic root dimension of WT and Marfan mice.

The diameter of the (A) aortic annulus, (B) sinus of Valsava and (C) sinotubular junction were significantly increased in Marfan mice versus WT. The larger aortic root diameter indicates significant aortic dilation. ** indicates $p < 0.01$, *** indicates $p < 0.001$.

3.3. Doppler Analysis of Aorta and Pulmonary Vessel

The velocity time integral (VTI) and the peak velocity of ascending and descending aorta were calculated from the pulsed-wave Doppler mode of an aortic arch view (Table 3.5). The ascending aortic VTI and peak velocities were significantly decreased by 36% (p = 0.002) and 25% (p = 0.01) in 12-month Marfan mice versus WT mice. Descending aortic peak velocity was significantly decreased by 28% in 12-month Marfan mice (p < 0.001) versus WT mice and by 18% in 12-month Marfan mice versus 6-month Marfan mice (p = 0.01), respectively. The descending aortic VTI was also decreased in Marfan mice verses WT at 6-month old (13%, p = 0.046) and 12-month old (34%, p < 0.001), and was decreased in 12-month old Marfan mice compared with the 6-month group (28%, p = 0.001) (Fig. 3.4).

The velocity time integral (VTI) and peak velocity of the pulmonary artery were calculated from the pulsed-wave Doppler mode of the LV long-axis view. As observed in the aorta, pulmonary VTI and peak velocity were significantly decreased by 18% (p = 0.02) and 15% (p = 0.01) in the 12-month Marfan mice versus WT mice.

Table 3.5. Doppler analysis of blood flow in aorta and pulmonary artery for WT and MFS mice.

Parameters (unit)	6 months group			12 months group			6 vs. 12 m
	WT	MFS	*P*	WT	MFS	*P*	MFS *P*
Asc aortic VTI (mm)	51.38 ± 2.49	48.76 ± 3.70	0.57	51.96 ± 4.01	33.47 ± 2.63	0.002**	0.005**
Asc aortic peak vel (mm/s)	1305.95 ± 61.25	1217.40 ± 110.81	0.50	1385.99 ± 94.77	1033.26 ± 75.45	0.01**	0.19
Desc aortic VTI (mm)	34.88 ± 1.68	30.47 ± 1.03	0.046*	33.22 ± 1.78	22.00 ± 1.63	<0.001***	<0.001***
Desc aortic peak vel (mm/s)	963.53 ± 55.76	857.68 ± 32.74	0.13	973.09 ± 34.07	699.04 ± 40.84	<0.001***	0.009**
Pulm artery VTI (mm)	26.85 ± 0.77	29.36 ± 1.48	0.16	27.44 ± 1.47	22.56 ± 0.97	0.02*	0.002**
Pulm artery peak vel (mm/s)	636.49 ± 18.39	676.29 ± 42.62	0.41	746.37 ± 29.9	637.78 ± 17.42	0.009**	0.42

All results are presented as Means ± SEM (n = 8 mice). * indicates $p < 0.05$, ** indicates $p < 0.01$, *** indicates $p < 0.001$. Asc, ascending; Desc, descending; Pulm, pulmonary; Vel, velocity; VTI, velocity time integral.

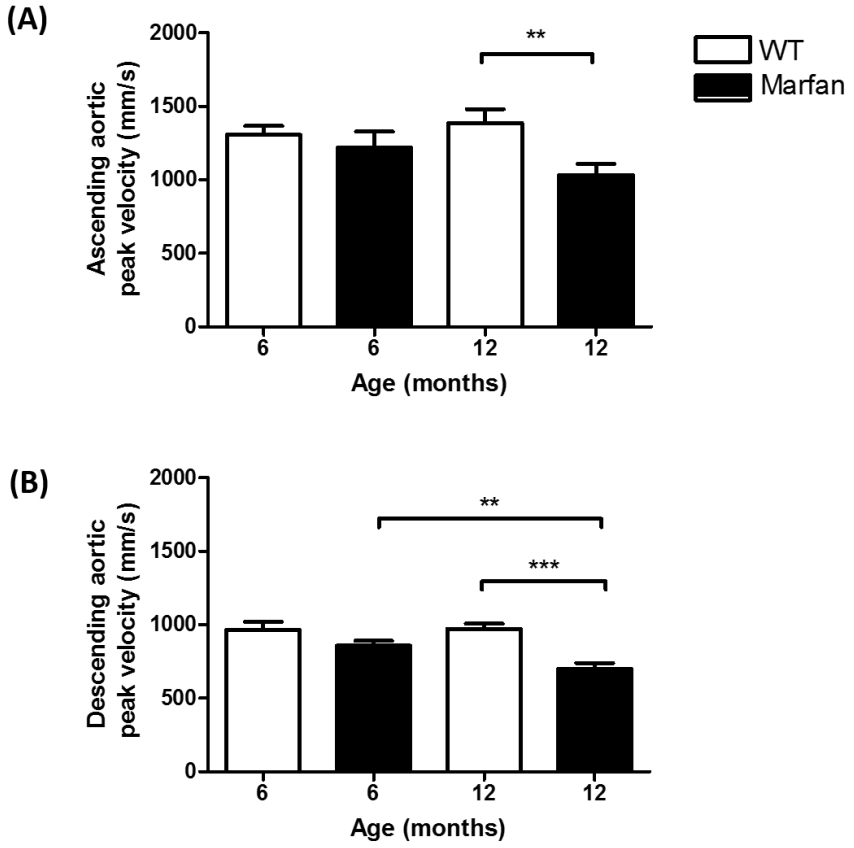

Figure 3.4. Echocardiographic assessment of (A) ascending aortic peak velocity (mm/s) and (B) descending aortic peak velocity (mm/s).

Peak velocity was calculated from pulsed-wave Doppler mode of an aortic arch view. **(A)** Ascending aortic peak velocity and **(B)** descending aortic peak velocity was significantly decreased in Marfan mice versus WT at 12-month groups. ** indicates $p < 0.01$, *** indicates $p < 0.001$.

3.4. Pulse Wave Velocity

Pulse wave (PW) velocity was significantly increased by 79% in 6-8 months old Marfan mice compared to WT ($p < 0.001$) and by 124% in 12-16 months Marfan mice compared to WT ($p = 0.001$), respectively. Figure 3.5 is a scatter diagram showing the relationship between age (x-axis) and PW velocity (y-axis) of Marfan and WT mice. PW velocity in Marfan mice increased directly proportional to age (R-squared =0.356, $p = 0.02$), but not in WT mice (R-squared =0.008, $p = 0.73$). The estimated regression equation is y = 0.45x + 275.49 in Marfan group as well as y = 0.06x + 187.01 in WT group.

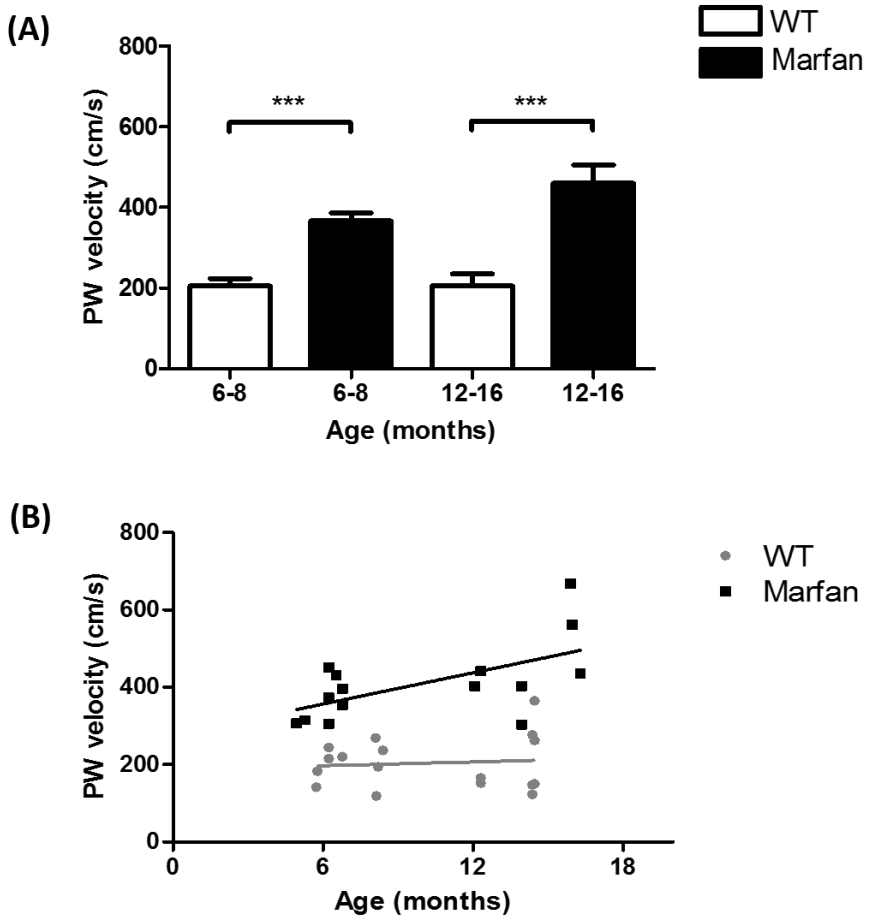

Figure 3.5. Pulse wave (PW) velocity of aortic arch.
(A) Aortic PW velocity of WT and Marfan mice from two age groups (6-8 months and 12-16 months group). **(B)** Correlations between age (x-axis) and PW velocity (y-axis) of WT (●) and Marfan (▪) mice. PW velocity in Marfan mice was directly proportional to age (R-squared =0.356, $p = 0.02$), but not in WT mice. *** indicates $p < 0.001$.

3.5. Strain Analysis

Strain analysis was applied on 12-month old Marfan and WT mice (n = 8). Regional and global strain and strain rate of the six segments in the LV were displayed in Table 3.6 and Table 3.7 The radial strain rates of the mid posterior and anterior free walls were significantly decreased by 28% (p = 0.007) and 26% (p = 0.04) in 12-month old Marfan mice compared with WT, respectively. The radial strain in mid posterior wall was reduced in 12-month old Marfan mice by 25% (p = 0.01) compare with WT.

Table 3.6. Comparison of Strain (%) between Marfan and WT mice (12 months old).

Parameters	Strain (%)		
	WT	MFS	*P*
Long Axis (Radial)			
Posterior wall base	21.82 ± 3.46	19.83 ± 3.07	0.67
Posterior wall mid	38.75 ± 2.81	28.91 ± 1.96	0.01*
Posterior wall apex	38.44 ± 4.50	31.48 ± 4.18	0.28
Anterior wall base	26.52 ± 5.09	29.18 ± 4.20	0.69
Anterior wall mid	35.59 ± 2.65	31.45 ± 3.64	0.37
Anterior wall apex	29.90 ± 3.20	26.56 ±3.06	0.46
Global LV wall	31.84 ±2.04	27.90 ± 2.07	0.20
Long Axis (Longitudinal)			
Posterior wall base	-10.17 ± 1.67	-9.92 ± 1.99	0.93
Posterior wall mid	-16.87 ± 1.37	-15.66 ± 1.27	0.53
Posterior wall apex	-23.86 ± 1.51	-22.39 ± 1.61	0.52
Anterior wall base	-9.61 ± 3.53	-11.87 ± 1.71	0.58
Anterior wall mid	-13.96 ± 1.29	-16.41 ± 2.30	0.37
Anterior wall apex	-21.57 ± 1.69	-19.34 ± 1.95	0.40
Global LV wall	-16.01 ± 1.03	-15.93 ± 0.85	0.96
Short Axis (Radial)			
Anterior free wall	41.55 ± 5.20	29.11 ± 2.33	0.05
Lateral wall	34.57 ± 10.27	35.86 ± 2.45	0.91
Posterior wall	45.29 ± 8.02	47.09 ± 5.66	0.86
Inferior free wall	36.71 ± 6.62	40.06 ± 7.16	0.74
Posterior septal wall	19.49 ± 3.60	26.63 ± 4.15	0.21
Anterior septum	34.48 ± 4.32	28.58 ± 4.16	0.34
Global LV wall	35.35 ± 4.33	34.55 ± 3.51	0.89
Short Axis (Circumferential)			
Anterior free wall	-28.27 ± 2.24	-28.57 ± 1.62	0.92
Lateral wall	-25.14 ± 1.87	-25.62 ± 1.84	0.86
Posterior wall	-22.52 ± 1.34	-22.48 ± 2.07	0.99
Inferior free wall	-24.40 ± 2.79	-25.95 ± 2.63	0.69
Posterior septal wall	-29.78 ± 3.50	-30.63 ± 3.48	0.87
Anterior septum	-29.41 ± 3.41	-32.09 ± 2.78	0.55
Global LV wall	-26.59 ± 2.30	-27.55 ± 1.98	0.75

All results are presented as Means ± SEM (n = 8 mice). * indicates $p < 0.05$, ** indicates $p < 0.01$.

Table 3.7. Comparison of Strain rate (1/s) between Marfan and WT mice (12 months old).

Parameters	Strain rate (1/s)		
	WT	MFS	P
Long Axis (Radial)			
Posterior wall base	6.37 ± 0.86	7.11 ± 0.64	0.51
Posterior wall mid	9.32 ± 0.69	6.75 ± 0.37	0.007**
Posterior wall apex	9.34 ± 0.50	9.10 ± 0.78	0.79
Anterior wall base	7.64 ± 0.79	7.04 ± 0.86	0.61
Anterior wall mid	8.49 ± 0.50	7.42 ± 0.79	0.28
Anterior wall apex	7.79 ± 0.57	8.32 ± 1.02	0.66
Global LV wall	8.16 ± 0.41	7.62 ± 0.42	0.38
Long Axis (Longitudinal)			
Posterior wall base	-6.20 ± 0.49	-6.27 ± 0.76	0.94
Posterior wall mid	-6.04 ± 0.68	-5.46 ± 0.53	0.52
Posterior wall apex	-8.48 ± 0.48	-7.47 ± 0.77	0.28
Anterior wall base	-5.22 ± 1.05	-6.09 ± 0.88	0.54
Anterior wall mid	-4.89 ± 0.36	-5.22 ± 0.47	0.59
Anterior wall apex	-7.02 ± 0.55	-6.79 ± 0.85	0.82
Global LV wall	-6.31 ± 0.43	-6.22 ± 0.44	0.88
Short Axis (Radial)			
Anterior free wall	9.48 ± 0.93	7.05 ± 0.47	0.04*
Lateral wall	9.78 ± 1.59	8.28 ± 0.70	0.41
Posterior wall	10.85 ± 1.45	9.36 ± 0.77	0.38
Inferior free wall	9.53 ± 0.97	9.00 ± 0.89	0.70
Posterior septal wall	7.67 ± 0.54	7.47 ± 0.61	0.80
Anterior septum	8.44 ± 0.66	7.61 ± 0.52	0.34
Global LV wall	9.29 ± 0.87	8.13 ± 0.38	0.25
Short Axis (Circumferential)			
Anterior free wall	-10.38 ± 0.88	-9.78 ± 1.15	0.68
Lateral wall	-9.44 ± 0.62	-9.02 ± 0.96	0.72
Posterior wall	-8.22 ± 0.38	-8.08 ± 0.69	0.86
Inferior free wall	-9.95 ± 1.11	-8.92 ± 0.93	0.49
Posterior septal wall	-11.14 ± 1.32	-10.70 ± 1.26	0.81
Anterior septum	-10.39 ± 1.15	-11.55 ± 1.75	0.59
Global LV wall	-9.92 ± 0.79	-9.67 ± 0.87	0.84

All results are presented as Means ± SEM (n = 8 mice). * indicates $p < 0.05$, ** indicates $p < 0.01$.

Chapter 4. Discussion

4.1. Echocardiographic Assessment of Aorta and Pulmonary Vessel

4.1.1. Aortic Stiffness

Elastic arterial stiffness is an important manifestation of Marfan syndrome. In patients with Marfan syndrome, the mutant fibillin-1 may lead to extracellular matrix remodeling in the aortic wall resulting in increased aortic stiffness (Kiotsekoglou, Moggridge et al. 2011). Increased aortic wall stiffening is associated with progressive aortic dilatation (Kroner, Scholte et al. 2013).

Aortic stiffness can be evaluated over a larger aortic segment by flow wave velocity or at a regional level by distensibility (Hirata, Triposkiadis et al. 1991). The aortic stiffness and diameters can be used to predict progressive aortic dilatation in Marfan patients (Nollen, Groenink et al. 2004). Previous studies have confirmed an increased aortic stiffness in Marfan patients by using echocardiography or magnetic resonance imaging (MRI) (Hirata, Triposkiadis et al. 1991, Savolainen, Keto et al. 1992, Jeremy, Huang et al. 1994, Groenink, de Roos et al. 2001, Kiotsekoglou, Moggridge et al. 2011, Kroner, Scholte et al. 2013).

Several measurements can be determined using echocardiography to evaluate stiffness level of aorta in Marfan patients, including pulse wave velocity, aortic distensibility and aortic stiffness index (Hirata, Triposkiadis et al. 1991). Pulse wave velocity can be calculated by the distance for the blood flow to travel (aortic length) divided by the transit time (Hirata, Triposkiadis et al. 1991). In this study aortic distensibility was measured from the changes in echocardiographic aortic diameters and brachial artery pressure with the formula: 2[(diastolic aortic diameter) - (systolic aortic

diameter)] / (diastolic aortic diameter) (pulse pressure) (Hirai, Sasayama et al. 1989). The aortic stiffness index was calculated by ln (systolic/diastolic blood pressure) / (aortic diameter change / aortic diastolic diameter), where ln is the natural logarithm (Stefanadis, Wooley et al. 1987).

In the study by Hirata *et al*. (1991) it was shown that Marfan patients (17 patients) have increased aortic stiffness index in the ascending and the abdominal aorta (10.9 ± 5.6 vs. 5.9 ± 2.2, p <0.005 and 7.1 ± 3.1 vs. 3.9 ± 1.2, p < 0.005, respectively) compared with normal subjects. Marfan patients had decreased aortic distensibility in the ascending and the abdominal aorta (2.9 ± 1.3 vs. 5.6 ± 1.4 cm^2 $dynes^{-1}$, p < 0.001 and 4.5 ± 2.1, vs. 7.7 ± 2.5, cm^2 $dynes^{-1}$, p < 0.001). The study also showed pulse wave velocity was more rapid in the patients than in the normal subjects (11.6 ± 2.5 vs. 9.5 ± 1.4 m/s, p < 0.01) (Hirata, Triposkiadis et al. 1991).

Another study by Jeremy et al that examined 170 Marfan patients reported that aortic distensibility was less in the Marfan group (2.6 ± 1.3 vs. 6.2 ± 2.1 cm^2 $dynes^{-1}$ 10^{-6}, p < 0.01), and aortic wall stiffness index (7.9 ± 3.4 vs. 2.8 ± 0.6, p < 0.01) and the calculated pulse wave velocity (621 ± 139 vs. 394 ± 62 cm/s, p < 0.01) were increased in the Marfan group than in the controls (Jeremy, Huang et al. 1994). Another study actually measured pulse wave velocity analysis was performed by Bradley, Potts *et al.* (2005) that showed that Marfan patients have increased pulse wave velocity compared with normal subjects (48.1 ± 7.0 vs. 35.7 ± 6.1 m/s, p < 0.0001) (Bradley, Potts et al. 2005).

In general, pulse wave velocity is proportional to the square root of the elastic modulus and inversely proportional to distensibility (Farrar, Green et al. 1980, Laogun and Gosling 1982). PW velocity has been demonstrated in different populations including elderly, hypertensive, diabetic and renal patients as an index of aortic stiffness (Cruickshank, Riste et al. 2002, Laurent, Katsahian et al. 2003, Sutton-Tyrrell, Najjar et al. 2005, Laurent, Cockcroft et al. 2006). In Marfan patients, it has been demonstrated that aortic stiffness was increased with age and aortic diameter (Jeremy, Huang et al. 1994). In other words, Marfan patients with stiffer and less distensible arteries present faster pulse waves traveling along the artery (Jeremy, Huang et al. 1994).

In our study, pulse wave velocity was significantly increased in 6-8 months Marfan mice compared with WT ($p < 0.001$) and in 12-16 months Marfan mice compared with WT ($p = 0.001$), respectively. Moreover, the pulse wave velocity in Marfan mice was directly proportional to age (R-squared =0.356, $p = 0.02$). These data are consistent with the notion that with increased age, the aorta becomes stiffer in the Marfan mice; thus, it increases the afterload placed on the heart and may eventually lead to cardiomyocyte abnormalities.

Our data are also consistent with previous studies, which applied the same PW velocity analysis methods on Marfan patients (Bradley, Potts et al. 2005). Our study confirms that PW velocity analysis by using 2-D and Doppler echocardiography can also be applied to the mouse for evaluating the level of aortic stiffness.

The difficulties of this analysis are that the aortic arch length in mice is small (~5.5 mm) compared with human (~5 cm). In addition, the transit time is very rapid due to the high heart rate of mice. However, with repeated measurements over ten cardiac cycles, the accuracy can be increased and thus human error can be reduced. These results support the fact that pulse wave velocity analysis as determined by ultrasound is an appropriate technique for the diagnosis and evaluation of aortic stiffness in the mouse model.

4.1.2. Aortic Root Dilation

Echocardiography is used routinely for Marfan patients' diagnosis and long term follow-up. Aortic root dilation and dissection are the earliest and the most common manifestations of cardiovascular Marfan disease, which are defined as the major criteria by the revised Ghent nosology (Loeys, Dietz et al. 2010). Progressive aortic root enlargement in Marfan patients usually initiated at the sinuses of Valsalva. Moreover, as the aortic root diameter is increased over 60 mm, there is a high chance of developing aortic valve regurgitation (Robinson and Godfrey 2004).

A literature review suggested that in adult males with Marfan syndrome, aortic dilatation is present in 83 %, aortic regurgitation in 53%, mitral valve prolapse in 57% and mitral valve regurgitation in 31% of the patients (Robinson and Godfrey 2004).

Brown O.R. *et al.* (1975) reported that aortic root dilatation was found in 60% of this group (74% of males, 33% of females) while mitral valve prolapse was found in 91% (87% of males, 100% of females) among 35 Marfan patients.

In our study, the aortic diameters that included the: aortic annulus, sinuses of Valsalva and sinotubular junction in the aortic root have been measured from the B-mode images. Our results show that Marfan mice have significantly increased diameters of the aortic annulus, sinuses of Valsalva and sinotubular junction by 18%, 19% and 13% for the 6-month group and 27%, 27% and 8% for the 12-month group, respectively. Our results are consistent with the notion that the aortic root lost its elasticity and progressively enlarges in Marfan mice, especially in sinuses of Valsalva and that these findings are consistent with previous studies of Marfan patients (Hirata, Triposkiadis et al. 1991, Nollen, Groenink et al. 2004, El-Hamamsy and Yacoub 2009).

The role of TGF-β in dilated aorta of Marfan mice has been clearly demonstrated by Habashi *et al.* (2006). Their study applied Verhoeff-Van Gieson (VVG) stain for elastin in the ascending aorta of the same MFS [Fbn1 (C1039G/+)] mice construct, and the results demonstrated diffuse disruption of elastic lamellae in the Marfan mice (14-week-old). In addition, immunohistochemistry (IH) revealed that the nuclear pSmad2, a marker for TGF-β signaling, was markedly increased in the Marfan mice (Habashi, Judge et al. 2006). More importantly, after being treated with TGF-β neutralizing antibody for 8 weeks, elastin fiber architecture and pSmad2 staining were observed to be normal in the Marfan mice, and thus aortic root dilatation is preventable. These data highlight the fact that TGF-β plays a critical role in the signaling in aortic dilation as well as other features of MFS (Habashi, Judge et al. 2006).

According to the Law of Laplace, the aortic wall stress is determined by the product of blood pressure and the aortic radius divided by the thickness of the aortic wall (Robinson and Godfrey 2004):

$$Aortic\ wall\ stress = \frac{(Aortic\ pressure\ \times radius)}{Aortic\ wall\ thickness}$$

In Marfan patients, the mutant fibrillin-1 in the aorta can cause aortic wall weakness and aortic dilatation, and thus increase the wall stress in the aorta. The abnormal fibrillin-1 causes dysfunction in the regulation of TGF-β1, and excessive TGF-β1 leads to progressive aortic root enlargement. This eventually leads to aorta dissection and rupture (Robinson and Godfrey 2004).

4.1.3. Decreased Peak Velocity and Velocity Time Integral

The peak velocity which was assessed by Doppler-mode is associated with vessel diameters. According to the Bernoulli principle, kinetic energy and pressure energy can be interconverted and thus total energy remains constant (Rhoades and Bell 2013). In the narrowed region of vessel, for instance vascular stenosis, the diameter decreases and the pressure within the vessel is decreased, resulting in an increased blood flow velocity (Rhoades and Bell 2013). The velocity time integral (VTI) can be used to estimate the “region of blood” flowing during this period. The VTI in the aortic valve area is a very important evaluation for aortic stenosis as higher VTI suggests a smaller valve area (Otto 2006).

In contrast, Marfan patients with dilated vessels present with a decreased peak velocity and VTI (Bradley, Potts et al. 2005). The results of this study also proved a significant decreased VTI and peak velocity in both the ascending and descending aortas. These results were more pronounced in the 12-month group which strongly suggests progressive dilation in the aorta of Marfan mice with aging.

Similarly, the pulmonary artery VTI and peak velocity were decreased significantly in Marfan mice in the 12-month but not 6-month group. Although we did not measure the diameter of the pulmonary vessels, the decreased artery VTI and peak velocity suggest the occurrence of a progressively dilated pulmonary artery in Marfan mice.

4.2. Echocardiographic Assessment of the Left Ventricular Structure and Function

4.2.1. Theories of Cardiomyopathy in Marfan Syndrome

Cardiomyopathy is a controversial finding in Marfan syndrome that is associated with the fibrillin-1 mutation (Alpendurada, Wong et al. 2010). The first case report published showing a Marfan patient presenting with evidence of hypertrophic cardiomyopathy occurred in 1985 (Fujiseki, Okuno et al. 1985).

Since fibrillin-1 is predominantly expressed in the proximal aorta, MFS media degeneration and consecutive aneurysmal formation are most prevalent in the ascending segment (Robinson and Godfrey 2004). Abnormal aortic elastic properties are manifested by increased aortic stiffness and decreased aortic distensibility, and these have been demonstrated in adults with Marfan syndrome (Hirata, Triposkiadis et al. 1991). Theoretically, the LV dysfunction could be an age-related phenomenon that results from the increased myocardial afterload that is caused by increased aortic stiffness (Cheung 2010).

According to the Law of Laplace, the factors that determine left ventricular wall stress are given as follows: (LV pressure × radius) / (2 × LV wall thickness) (Lorell and Carabello 2000). Therefore, an increase in LV pressure or lumen diameter can lead to an increase in wall thickness.

In Marfan mice, the increased aortic stiffness leads to greater afterload placed on the heart, forcing to contract more vigorously to accommodate the stiffened artery, resulting in an increase of LV pressure (Nollen, Groenink et al. 2004). The increased valve regurgitation caused by the cardiac valve abnormalities can also lead to increased LV pressure (Pyeritz 2000). Consequently, the LV wall thickness is increased in Marfan mice as a compensatory mechanism to decrease wall stress. Over time, this increased afterload placed on the heart may cause LV hypertrophy and eventually heart failure.

However, there is still a debate whether a primary cardiomyopathy exists, since fibrillin-1 is also present in the myocardium. A study described a mouse model with

fibrillin-1 mutation associated with hypertrophic cardiomyopathy (Siracusa, McGrath et al. 1996). Despite the fact that most cases of heart failure were caused by heart valve incompetence instead of primary myocardial tissue dysfunction, some studies have reported that the Marfan patients had dilated cardiomyopathy in the absence of severe valvular dysfunction (Chatrath, Beauchesne et al. 2003, Yetman, Bornemeier et al. 2003, Kahveci, Erkol et al. 2010). Moreover, some cases of Marfan patients have presented with ventricular connective tissue abnormality including elongation, abnormal insertion and spontaneous rupture of the chordae tendinae and dilation of the annulus fibrosus (el Habbal 1992). These findings suggest that the abnormal extracellular connective tissue matrix of the myocardium may also contribute to the LV dysfunction in Marfan patients.

4.2.2. Left Ventricular Diastolic Dysfunction

Diastolic dysfunction due to the abnormal recoil of the fibrillin-containing myocardial interstitium has been reported in case series of Marfan patients (Das, Taylor et al. 2006, Angtuaco, Vyas et al. 2012). Abnormal LV elastic recoil, marked by impaired relaxation, presented early in life suggests an intrinsic abnormality of the myocardium.

Another study reported a significant increase in left ventricular end-diastolic diameter, deceleration time (DT) and isovolumic relaxation time (IVRT) as well as significantly decreased mitral valve E wave velocity and E/A ratio in young Marfan patients compared with healthy controls (Das, Taylor et al. 2006). These data suggest the presence of LV diastolic dysfunction in Marfan patients. Furthermore, the authors indicated that these abnormalities were noted in all age groups and there was no correlation between predicted aortic root size and any measure of diastolic performance, suggesting that diastolic alterations may be a result of an inherent myocardial abnormality rather than occurring as a result of impaired aortic compliance.

In our study, the LV interventricular septal thickness and LV mass were increased significantly in the 6-month old Marfan mice, as well as the anterior and posterior wall were increased significantly in the 12-month old Marfan mice. Furthermore, the significantly decreased E velocity, E/A ratio and prolonged IVRT were observed in the Marfan mice group at both 6-months and 12-months of age. The lower E velocity and

prolonged IVRT are indicative of impaired relaxation, which is grade I diastolic dysfunction in Marfan mice (Little and Oh 2009). The magnitude of the E-wave decreased is triggered by a stiff ventricle which impairs early filling of the ventricle. Besides, it takes longer for atrial pressure to be high enough to initiate filling, and thus prolonging the IVRT (Little and Oh 2009).

Our data suggest that the Marfan mice heart exhibits diastolic dysfunction and a tendency towards cardiac hypertrophy which are consistent with clinical findings (Das, Taylor et al. 2006, Angtuaco, Vyas et al. 2012). However, since the aortic dilation and stiffness also occurred in both 6-month and 12 month groups, it is not clear whether the increased LV muscle mass and abnormal diastolic function are due to the abnormal after-load caused either by increased aortic stiffness or by abnormal myocardial connective tissue.

4.2.3. Left Ventricular Dilation

Our study illustrates that the end diastolic volume was increased significantly by 21% compared with WT (p = 0.03) in the 6-month group, and the stroke volume was also increased by 30% in the 6-month Marfan mice (p = 0.005). According to Frank-Starling mechanism, increased end-diastolic volume (preload) can lead to cardiac myocyte stretching and increase the sarcomere length, which causes an increase in force generation. This mechanism enables the heart to eject the additional volume and thus increasing stroke volume (Bers 2001).

However, since the afterload was also increased in the Marfan mice, increase in the stroke volume should be attenuated. A possible reason is that the stroke volumes that we calculated were based on the LV lumen diameters (EDV - ESV). Under normal circumstances, all of the ejected blood should be pumped into the aorta. In Marfan syndrome, there is a high probability of having mitral valve prolapse and regurgitation, which means part of the blood might flow back into atrium (Tsipouras and Devereux 1993, Lebreiro, Martins et al. 2010). In this case, a better way to measure the stroke volume is using SV = VTI × CSA, where VTI stands for the velocity time integral of the

left ventricular outflow tract and CSA stands for valve orifice cross sectional area (Hakki, Iskandrian et al. 1981).

To further understand the structural properties of the Marfan mouse heart, we collaborated with Dr. Sarunic's lab at Simon Fraser University to apply optical coherence tomography (OCT) on the 12-month old Marfan mouse isolated heart. OCT provides higher resolution (10 μm) and lower penetrance (1 to 2 mm) compared with our ultrasound system. Both 2D and 3D LV volumes were acquired by OCT in order to compare the 2D measurement that were acquired in echo. The results demonstrated that the 2D LV volume in Marfan mice were lower than the 3D volume, indicated that our M-mode equation of LV volume in the 12-month-old may be inaccurate and result in an underestimation of volume. The reason might be the development of myocardial deformation in the 12-months old Marfan mice that changed the morphology of the heart and thus the LV volume was difficult to estimate from a single plane.

4.2.4. Left Ventricular Deformation

Strain analysis was used for investigating the regional myocardial deformation in the heart. Previous studies found that Marfan patients exhibited decreased strain and strain rate, suggesting that Marfan patients exhibit regional myocardial deformation and abnormalities in the left ventricle (Kiotsekoglou, Saha et al. 2011, Angtuaco, Vyas et al. 2012)

A pervious study demonstrated that adult Marfan patients LV radial and LV and right ventricular (RV) long-axis strain (%) were reduced (70 ± 17 vs 93 ± 10; 19 ± 2 vs 25 ± 2; 30 ± 9 vs 36 ± 8, respectively, $p < 0.001$) compared with normal subjects. Strain rate measurements were also reduced ($p < 0.001$) (Kiotsekoglou, Saha et al. 2011). Another study indicated that children and young Marfan patients ($y < 30$) had lower regional radial and circumferential strain rates, but there were no significant differences in strain between the groups (Angtuaco, Vyas et al. 2012).

Myocardial deformation abnormalities in Marfan syndrome presumably is due to the remodeling of the extracellular matrix and abnormalities in the TGF β1 biological pathway caused by the mutant fibrillin-1; this in turn results in reduced functionality in the

LV. However, increased aortic stiffness may be one of the reasons for the existence of segmental ventricular abnormalities (Angtuaco, Vyas et al. 2012).

In our study, the radial strain rate of the mid posterior and anterior free walls were significantly decreased in the 12-month old Marfan mice compared with WT ($p < 0.05$). The strain in the mid posterior wall was reduced in the 12-month old Marfan mice as well. Strain and strain rate in other LV segments also decreased in the Marfan group but did not reach a significant level. However, some of the Marfan mice displayed abnormal, slow contraction in the B-mode video, and this caused the increase in variance in the Marfan group. Therefore, we may see more significance in the differences if we increase the sample numbers.

4.3. The Significance of the Study

The abnormal heart morphology of 6-month and 12-month old MFS [Fbn1 (C1039G/+)] mice was well characterized in our study by using high resolution ultrasound, and the results provide important insight as to how this particular mutation causes the various manifestation in the human Marfan heart.

This study clearly demonstrated an increased pulse wave velocity, which is strongly associated with age in the Marfan mice. The results are indicative of a progressively increased aortic stiffness in the Marfan mice. Moreover, it also proved that PW velocity measurement can be successfully used for quantitating the level of aortic stiffness in the mouse model.

Two different ages of Marfan mice groups were evaluated in this study. Therefore, we are able to extrapolate the results to humans for an interpretation of the effects of aging in Marfan patients. Furthermore, this echo system has been proved to be useful in the detection of changes in cardiac structure and function in Marfan syndrome mice model. Thus, it can be used for evaluating the impact of drug therapy (e.g., losartan) on this animal model, and to predict human outcomes in the future.

Chapter 5. Conclusions

Our results indicate that Marfan mice have significantly increased LV mass and wall thickness in both 6- and 12-month groups, which indicates that the Marfan mouse exhibits a tendency towards hypertrophic cardiomyopathy. The lower E filling velocity and E/A ratio are suggestive of left ventricular diastolic dysfunction in MFS mice and were also observable in both age groups. The progressively larger aortic root diameter and higher PW velocity show significant aortic dilation and central aortic stiffness in the MFS mice, which are associated with LV hypertrophy and diastolic stiffness. However, it is not clear whether the increased LV muscle mass and abnormal diastolic function are due to the abnormal after-load caused either by increased aortic stiffness or by abnormal myocardial connective tissue.

References

Alpendurada, F., J. Wong, A. Kiotsekoglou, W. Banya, A. Child, S. K. Prasad, D. J. Pennell and R. H. Mohiaddin (2010). "Evidence for Marfan cardiomyopathy." Eur J Heart Fail **12**(10): 1085-1091.

Angtuaco, M. J., H. V. Vyas, S. Malik, B. N. Holleman, J. M. Gossett and R. Sachdeva (2012). "Early detection of cardiac dysfunction by strain and strain rate imaging in children and young adults with marfan syndrome." J Ultrasound Med **31**(10): 1609-1616.

Arnlov, J., E. Ingelsson, U. Riserus, B. Andren and L. Lind (2004). "Myocardial performance index, a Doppler-derived index of global left ventricular function, predicts congestive heart failure in elderly men." Eur Heart J **25**(24): 2220-2225.

Arslan-Kirchner, M., Y. von Kodolitsch and J. Schmidtke (2008). "The importance of genetic testing in the clinical management of patients with Marfan syndrome and related disorders." Dtsch Arztebl Int **105**(27): 483-491.

Bers, D. M. (2001). Excitation-contraction coupling and cardiac contractile force. Dordrecht ; Boston, Kluwer Academic Publishers.

Booms, P., A. Ney, F. Barthel, G. Moroy, D. Counsell, C. Gille, G. Guo, R. Pregla, S. Mundlos, A. J. Alix and P. N. Robinson (2006). "A fibrillin-1-fragment containing the elastin-binding-protein GxxPG consensus sequence upregulates matrix metalloproteinase-1: biochemical and computational analysis." J Mol Cell Cardiol **40**(2): 234-246.

Bradley, T. J., J. E. Potts, M. T. Potts, A. M. DeSouza and G. G. Sandor (2005). "Echocardiographic Doppler assessment of the biophysical properties of the aorta in pediatric patients with the Marfan syndrome." Am J Cardiol **96**(9): 1317-1321.

Canadas, V., I. Vilacosta, I. Bruna and V. Fuster (2010). "Marfan syndrome. Part 1: pathophysiology and diagnosis." Nat Rev Cardiol **7**(5): 256-265.

Chamberlain, J. S. (2007). "ACE inhibitor bulks up muscle." Nat Med **13**(2): 125-126.

Chatrath, R., L. M. Beauchesne, H. M. Connolly, V. V. Michels and D. J. Driscoll (2003). "Left ventricular function in the Marfan syndrome without significant valvular regurgitation." Am J Cardiol **91**(7): 914-916.

Chaudhry, S. S., S. A. Cain, A. Morgan, S. L. Dallas, C. A. Shuttleworth and C. M. Kielty (2007). "Fibrillin-1 regulates the bioavailability of TGFbeta1." J Cell Biol **176**(3): 355-367.

Cheung, M. C., P. B. Spalding, J. C. Gutierrez, W. Balkan, N. Namias, L. G. Koniaris and T. A. Zimmers (2009). "Body surface area prediction in normal, hypermuscular, and obese mice." J Surg Res **153**(2): 326-331.

Cheung, Y. F. (2010). "Arterial stiffness in the young: assessment, determinants, and implications." Korean Circ J **40**(4): 153-162.

Chiu, H. H., M. H. Wu, J. K. Wang, C. W. Lu, S. N. Chiu, C. A. Chen, M. T. Lin and F. C. Hu (2013). "Losartan added to beta-blockade therapy for aortic root dilation in Marfan syndrome: a randomized, open-label pilot study." Mayo Clin Proc **88**(3): 271-276.

Cohen, P. R. and P. Schneiderman (1989). "Clinical manifestations of the Marfan syndrome." Int J Dermatol **28**(5): 291-299.

Cohn, R. D., C. van Erp, J. P. Habashi, A. A. Soleimani, E. C. Klein, M. T. Lisi, M. Gamradt, C. M. ap Rhys, T. M. Holm, B. L. Loeys, F. Ramirez, D. P. Judge, C. W. Ward and H. C. Dietz (2007). "Angiotensin II type 1 receptor blockade attenuates TGF-beta-induced failure of muscle regeneration in multiple myopathic states." Nat Med **13**(2): 204-210.

Constantinides, C., R. Mean and B. J. Janssen (2011). "Effects of isoflurane anesthesia on the cardiovascular function of the C57BL/6 mouse." ILAR J **52**: e21-31.

Cruickshank, K., L. Riste, S. G. Anderson, J. S. Wright, G. Dunn and R. G. Gosling (2002). "Aortic pulse-wave velocity and its relationship to mortality in diabetes and glucose intolerance: an integrated index of vascular function?" Circulation **106**(16): 2085-2090.

Das, B. B., A. L. Taylor and A. T. Yetman (2006). "Left ventricular diastolic dysfunction in children and young adults with Marfan syndrome." Pediatr Cardiol **27**(2): 256-258.

De Paepe, A., R. B. Devereux, H. C. Dietz, R. C. Hennekam and R. E. Pyeritz (1996). "Revised diagnostic criteria for the Marfan syndrome." Am J Med Genet **62**(4): 417-426.

Devereux, R. B. and N. Reichek (1977). "Echocardiographic determination of left ventricular mass in man. Anatomic validation of the method." Circulation **55**(4): 613-618.

Dietz, H. C., G. R. Cutting, R. E. Pyeritz, C. L. Maslen, L. Y. Sakai, G. M. Corson, E. G. Puffenberger, A. Hamosh, E. J. Nanthakumar, S. M. Curristin and et al. (1991). "Marfan syndrome caused by a recurrent de novo missense mutation in the fibrillin gene." Nature **352**(6333): 337-339.

Dietz, H. C., B. Loeys, L. Carta and F. Ramirez (2005). "Recent progress towards a molecular understanding of Marfan syndrome." Am J Med Genet C Semin Med Genet **139C**(1): 4-9.

El-Hamamsy, I. and M. H. Yacoub (2009). "Cellular and molecular mechanisms of thoracic aortic aneurysms." Nat Rev Cardiol **6**(12): 771-786.

el Habbal, M. H. (1992). "Cardiovascular manifestations of Marfan's syndrome in the young." Am Heart J **123**(3): 752-757.

Faivre, L., G. Collod-Beroud, B. L. Loeys, A. Child, C. Binquet, E. Gautier, B. Callewaert, E. Arbustini, K. Mayer, M. Arslan-Kirchner, A. Kiotsekoglou, P. Comeglio, N. Marziliano, H. C. Dietz, D. Halliday, C. Beroud, C. Bonithon-Kopp, M. Claustres, C. Muti, H. Plauchu, P. N. Robinson, L. C. Ades, A. Biggin, B. Benetts, M. Brett, K. J. Holman, J. De Backer, P. Coucke, U. Francke, A. De Paepe, G. Jondeau and C. Boileau (2007). "Effect of mutation type and location on clinical outcome in 1,013 probands with Marfan syndrome or related phenotypes and FBN1 mutations: an international study." Am J Hum Genet **81**(3): 454-466.

Farrar, D. J., H. D. Green, W. D. Wagner and M. G. Bond (1980). "Reduction in pulse wave velocity and improvement of aortic distensibility accompanying regression of atherosclerosis in the rhesus monkey." Circ Res **47**(3): 425-432.

Freed, C. and N. B. Schiller (1977). "Echocardiographic findings in Marfan's syndrome." West J Med **126**(2): 87-90.

Fujiseki, Y., K. Okuno, M. Tanaka, M. Shimada, M. Takahashi and K. Kawanishi (1985). "Myocardial involvement in the Marfan syndrome." Jpn Heart J **26**(6): 1043-1050.

Gao, S., D. Ho, D. E. Vatner and S. F. Vatner (2011). "Echocardiography in Mice." Curr Protoc Mouse Biol **1**: 71-83.

Gould, R. A., R. Sinha, H. Aziz, R. Rouf, H. C. Dietz, 3rd, D. P. Judge and J. Butcher (2012). "Multi-scale biomechanical remodeling in aging and genetic mutant murine mitral valve leaflets: insights into Marfan syndrome." PLoS One **7**(9): e44639.

Gressner, A. M., R. Weiskirchen, K. Breitkopf and S. Dooley (2002). "Roles of TGF-beta in hepatic fibrosis." Front Biosci **7**: d793-807.

Groenink, M., A. de Roos, B. J. Mulder, B. Verbeeten, Jr., J. Timmermans, A. H. Zwinderman, J. A. Spaan and E. E. van der Wall (2001). "Biophysical properties of the normal-sized aorta in patients with Marfan syndrome: evaluation with MR flow mapping." Radiology **219**(2): 535-540.

Groenink, M., A. W. den Hartog, R. Franken, T. Radonic, V. de Waard, J. Timmermans, A. J. Scholte, M. P. van den Berg, A. M. Spijkerboer, H. A. Marquering, A. H. Zwinderman and B. J. Mulder (2013). "Losartan reduces aortic dilatation rate in adults with Marfan syndrome: a randomized controlled trial." Eur Heart J **34**(45): 3491-3500.

Guo, G., P. Booms, M. Halushka, H. C. Dietz, A. Ney, S. Stricker, J. Hecht, S. Mundlos and P. N. Robinson (2006). "Induction of macrophage chemotaxis by aortic extracts of the mgR Marfan mouse model and a GxxPG-containing fibrillin-1 fragment." Circulation **114**(17): 1855-1862.

Habashi, J. P., D. P. Judge, T. M. Holm, R. D. Cohn, B. L. Loeys, T. K. Cooper, L. Myers, E. C. Klein, G. Liu, C. Calvi, M. Podowski, E. R. Neptune, M. K. Halushka, D. Bedja, K. Gabrielson, D. B. Rifkin, L. Carta, F. Ramirez, D. L. Huso and H. C. Dietz (2006). "Losartan, an AT1 antagonist, prevents aortic aneurysm in a mouse model of Marfan syndrome." Science **312**(5770): 117-121.

Hakki, A. H., A. S. Iskandrian, C. E. Bemis, D. Kimbiris, G. S. Mintz, B. L. Segal and C. Brice (1981). "A simplified valve formula for the calculation of stenotic cardiac valve areas." Circulation **63**(5): 1050-1055.

Hirai, T., S. Sasayama, T. Kawasaki and S. Yagi (1989). "Stiffness of systemic arteries in patients with myocardial infarction. A noninvasive method to predict severity of coronary atherosclerosis." Circulation **80**(1): 78-86.

Hirata, K., F. Triposkiadis, E. Sparks, J. Bowen, C. F. Wooley and H. Boudoulas (1991). "The Marfan syndrome: abnormal aortic elastic properties." J Am Coll Cardiol **18**(1): 57-63.

Hiratzka, L. F., G. L. Bakris, J. A. Beckman, R. M. Bersin, V. F. Carr, D. E. Casey, Jr., K. A. Eagle, L. K. Hermann, E. M. Isselbacher, E. A. Kazerooni, N. T. Kouchoukos, B. W. Lytle, D. M. Milewicz, D. L. Reich, S. Sen, J. A. Shinn, L. G. Svensson, D. M. Williams, G. American College of Cardiology Foundation/American Heart Association Task Force on Practice, S. American Association for Thoracic, R. American College of, A. American Stroke, A. Society of Cardiovascular, A. Society for Cardiovascular, Interventions, R. Society of Interventional, S. Society of Thoracic and M. Society for Vascular (2010). "2010 ACCF/AHA/AATS/ACR/ASA/SCA/SCAI/SIR/STS/SVM guidelines for the diagnosis and management of patients with Thoracic Aortic Disease: a report of the American College of Cardiology Foundation/American Heart Association Task Force on Practice Guidelines, American Association for Thoracic Surgery, American College of Radiology, American Stroke Association, Society of Cardiovascular Anesthesiologists, Society for Cardiovascular Angiography and Interventions, Society of Interventional Radiology, Society of Thoracic Surgeons, and Society for Vascular Medicine." Circulation **121**(13): e266-369.

Jeremy, R. W., H. Huang, J. Hwa, H. McCarron, C. F. Hughes and J. G. Richards (1994). "Relation between age, arterial distensibility, and aortic dilatation in the Marfan syndrome." Am J Cardiol **74**(4): 369-373.

Judge, D. P., N. J. Biery, D. R. Keene, J. Geubtner, L. Myers, D. L. Huso, L. Y. Sakai and H. C. Dietz (2004). "Evidence for a critical contribution of haploinsufficiency in the complex pathogenesis of Marfan syndrome." J Clin Invest **114**(2): 172-181.

Judge, D. P. and H. C. Dietz (2005). "Marfan's syndrome." Lancet **366**(9501): 1965-1976.

Kahveci, G., A. Erkol and F. Yilmaz (2010). "Dilated cardiomyopathy in a patient with Marfan syndrome accompanied by chronic type A aortic dissection and right atrial thrombus." Intern Med **49**(23): 2583-2586.

Keane, M. G. and R. E. Pyeritz (2008). "Medical management of Marfan syndrome." Circulation **117**(21): 2802-2813.

Kiotsekoglou, A., A. Bajpai, B. H. Bijnens, V. Kapetanakis, G. Athanassopoulos, J. C. Moggridge, M. J. Mullen, D. K. Nassiri, J. Camm, G. R. Sutherland and A. H. Child (2008). "Early impairment of left ventricular long-axis systolic function demonstrated by reduced atrioventricular plane displacement in patients with Marfan syndrome." Eur J Echocardiogr **9**(5): 605-613.

Kiotsekoglou, A., J. C. Moggridge, S. K. Saha, V. Kapetanakis, M. Govindan, F. Alpendurada, M. J. Mullen, J. Camm, G. R. Sutherland, B. H. Bijnens and A. H. Child (2011). "Assessment of aortic stiffness in marfan syndrome using two-dimensional and Doppler echocardiography." Echocardiography **28**(1): 29-37.

Kiotsekoglou, A., S. Saha, J. C. Moggridge, V. Kapetanakis, M. Govindan, F. Alpendurada, M. J. Mullen, D. K. Nassiri, J. Camm, G. R. Sutherland, B. H. Bijnens and A. Child (2011). "Impaired biventricular deformation in Marfan syndrome: a strain and strain rate study in adult unoperated patients." Echocardiography **28**(4): 416-430.

Kiotsekoglou, A., S. K. Saha, J. C. Moggridge, V. Kapetanakis, B. H. Bijnens, M. J. Mullen, J. Camm, G. R. Sutherland, I. B. Wilkinson and A. H. Child (2010). "Effect of aortic stiffness on left ventricular long-axis systolic function in adults with Marfan syndrome." Hellenic J Cardiol **51**(6): 501-511.

Kroner, E. S., A. J. Scholte, P. J. de Koning, P. J. van den Boogaard, L. J. Kroft, R. J. van der Geest, Y. Hilhorst-Hofstee, H. J. Lamb, H. M. Siebelink, B. J. Mulder, M. Groenink, T. Radonic, E. E. van der Wall, A. de Roos, J. H. Reiber and J. J. Westenberg (2013). "MRI-assessed regional pulse wave velocity for predicting absence of regional aorta luminal growth in marfan syndrome." Int J Cardiol **167**(6): 2977-2982.

Ladouceur, M., C. Fermanian, J. M. Lupoglazoff, T. Edouard, Y. Dulac, P. Acar, S. Magnier and G. Jondeau (2007). "Effect of beta-blockade on ascending aortic dilatation in children with the Marfan syndrome." Am J Cardiol **99**(3): 406-409.

Laogun, A. A. and R. G. Gosling (1982). "In vivo arterial compliance in man." Clin Phys Physiol Meas **3**(3): 201-212.

Laurent, S., J. Cockcroft, L. Van Bortel, P. Boutouyrie, C. Giannattasio, D. Hayoz, B. Pannier, C. Vlachopoulos, I. Wilkinson, H. Struijker-Boudier and A. European Network for Non-invasive Investigation of Large (2006). "Expert consensus document on arterial stiffness: methodological issues and clinical applications." Eur Heart J **27**(21): 2588-2605.

Laurent, S., S. Katsahian, C. Fassot, A. I. Tropeano, I. Gautier, B. Laloux and P. Boutouyrie (2003). "Aortic stiffness is an independent predictor of fatal stroke in essential hypertension." Stroke **34**(5): 1203-1206.

Lebreiro, A., E. Martins, C. Cruz, J. Almeida, M. J. Maciel, J. C. Cardoso and C. A. Lima (2010). "Marfan syndrome: clinical manifestations, pathophysiology and new outlook on drug therapy." Rev Port Cardiol **29**(6): 1021-1036.

Lindsay, M. E. and H. C. Dietz (2011). "Lessons on the pathogenesis of aneurysm from heritable conditions." Nature **473**(7347): 308-316.

Little, W. C. and J. K. Oh (2009). "Echocardiographic evaluation of diastolic function can be used to guide clinical care." Circulation **120**(9): 802-809.

Loeys, B. L., H. C. Dietz, A. C. Braverman, B. L. Callewaert, J. De Backer, R. B. Devereux, Y. Hilhorst-Hofstee, G. Jondeau, L. Faivre, D. M. Milewicz, R. E. Pyeritz, P. D. Sponseller, P. Wordsworth and A. M. De Paepe (2010). "The revised Ghent nosology for the Marfan syndrome." J Med Genet **47**(7): 476-485.

Lorell, B. H. and B. A. Carabello (2000). "Left ventricular hypertrophy: pathogenesis, detection, and prognosis." Circulation **102**(4): 470-479.

Ludders, J. W. (1992). "Advantages and guidelines for using isoflurane." Vet Clin North Am Small Anim Pract **22**(2): 328-331.

Matt, P. and F. Eckstein (2011). "Novel pharmacological strategies to prevent aortic complications in Marfan syndrome." J Geriatr Cardiol **8**(4): 254-257.

Matt, P., F. Schoenhoff, J. Habashi, T. Holm, C. Van Erp, D. Loch, O. D. Carlson, B. F. Griswold, Q. Fu, J. De Backer, B. Loeys, D. L. Huso, N. B. McDonnell, J. E. Van Eyk and H. C. Dietz (2009). "Circulating transforming growth factor-beta in Marfan syndrome." Circulation **120**(6): 526-532.

Maumenee, I. H. (1981). "The eye in the Marfan syndrome." Trans Am Ophthalmol Soc **79**: 684-733.

Nelson, L. B. and I. H. Maumenee (1982). "Ectopia lentis." Surv Ophthalmol **27**(3): 143-160.

Nihoyannopoulos, P. and J. Kisslo (2009). Echocardiography, Springer London.

Nollen, G. J., M. Groenink, J. G. Tijssen, E. E. Van Der Wall and B. J. Mulder (2004). "Aortic stiffness and diameter predict progressive aortic dilatation in patients with Marfan syndrome." Eur Heart J **25**(13): 1146-1152.

Otto, C. M. (2006). "Valvular aortic stenosis: disease severity and timing of intervention." J Am Coll Cardiol **47**(11): 2141-2151.

Pearson, G. D., R. Devereux, B. Loeys, C. Maslen, D. Milewicz, R. Pyeritz, F. Ramirez, D. Rifkin, L. Sakai, L. Svensson, A. Wessels, J. Van Eyk, H. C. Dietz, L. National Heart, I. Blood and G. National Marfan Foundation Working (2008). "Report of the National Heart, Lung, and Blood Institute and National Marfan Foundation Working Group on research in Marfan syndrome and related disorders." Circulation **118**(7): 785-791.

Pyeritz, R. E. (2000). "The Marfan syndrome." Annu Rev Med **51**: 481-510.

Ram, R., D. M. Mickelsen, C. Theodoropoulos and B. C. Blaxall (2011). "New approaches in small animal echocardiography: imaging the sounds of silence." Am J Physiol Heart Circ Physiol **301**(5): H1765-1780.

Rhoades, R. and D. R. Bell (2013). Medical physiology : principles for clinical medicine. Philadelphia, Wolters Kluwer Health/Lippincott Williams & Wilkins.

Robinson, P. N. and M. Godfrey (2004). Marfan syndrome : a primer for clinicians and scientists. Georgetown, Tex.

New York, N.Y., Landes Bioscience/Eurekah.com ;

Kluwer Academic/Plenum.

Roth, D. M., J. S. Swaney, N. D. Dalton, E. A. Gilpin and J. Ross, Jr. (2002). "Impact of anesthesia on cardiac function during echocardiography in mice." Am J Physiol Heart Circ Physiol **282**(6): H2134-2140.

Salim, M. A., B. S. Alpert, J. C. Ward and R. E. Pyeritz (1994). "Effect of beta-adrenergic blockade on aortic root rate of dilation in the Marfan syndrome." Am J Cardiol **74**(6): 629-633.

Savolainen, A., P. Keto, P. Hekali, L. Nisula, I. Kaitila, M. Viitasalo, V. P. Poutanen, C. G. Standertskjold-Nordenstam and M. Kupari (1992). "Aortic distensibility in children with the Marfan syndrome." Am J Cardiol **70**(6): 691-693.

Shores, J., K. R. Berger, E. A. Murphy and R. E. Pyeritz (1994). "Progression of aortic dilatation and the benefit of long-term beta-adrenergic blockade in Marfan's syndrome." N Engl J Med **330**(19): 1335-1341.

Siracusa, L. D., R. McGrath, Q. Ma, J. J. Moskow, J. Manne, P. J. Christner, A. M. Buchberg and S. A. Jimenez (1996). "A tandem duplication within the fibrillin 1 gene is associated with the mouse tight skin mutation." Genome Res **6**(4): 300-313.

Solomon, S. D. and B. E. Bulwer (2007). Essential echocardiography : a practical handbook with DVD. Totowa, N.J., Humana Press.

Stefanadis, C., C. F. Wooley, C. A. Bush, A. J. Kolibash and H. Boudoulas (1987). "Aortic distensibility abnormalities in coronary artery disease." Am J Cardiol **59**(15): 1300-1304.

Stypmann, J., M. A. Engelen, C. Troatz, M. Rothenburger, L. Eckardt and K. Tiemann (2009). "Echocardiographic assessment of global left ventricular function in mice." Lab Anim **43**(2): 127-137.

Sutton-Tyrrell, K., S. S. Najjar, R. M. Boudreau, L. Venkitachalam, V. Kupelian, E. M. Simonsick, R. Havlik, E. G. Lakatta, H. Spurgeon, S. Kritchevsky, M. Pahor, D. Bauer, A. Newman and A. B. C. S. Health (2005). "Elevated aortic pulse wave velocity, a marker of arterial stiffness, predicts cardiovascular events in well-functioning older adults." Circulation **111**(25): 3384-3390.

Taylor, K. J. and S. Holland (1990). "Doppler US. Part I. Basic principles, instrumentation, and pitfalls." Radiology **174**(2): 297-307.

Tsipouras, P. and R. B. Devereux (1993). "Marfan syndrome: genetic basis and clinical manifestations." Semin Dermatol **12**(3): 219-228.

Wood, J. R., D. Bellamy, A. H. Child and K. M. Citron (1984). "Pulmonary disease in patients with Marfan syndrome." Thorax **39**(10): 780-784.

Wu, J., L. Bu, H. Gong, G. Jiang, L. Li, H. Ma, N. Zhou, L. Lin, Z. Chen, Y. Ye, Y. Niu, A. Sun, J. Ge and Y. Zou (2010). "Effects of heart rate and anesthetic timing on high-resolution echocardiographic assessment under isoflurane anesthesia in mice." J Ultrasound Med **29**(12): 1771-1778.

Xiong, W., T. Meisinger, R. Knispel, J. M. Worth and B. T. Baxter (2012). "MMP-2 regulates Erk1/2 phosphorylation and aortic dilatation in Marfan syndrome." Circ Res **110**(12): e92-e101.

Yetman, A. T., R. A. Bornemeier and B. W. McCrindle (2003). "Long-term outcome in patients with Marfan syndrome: is aortic dissection the only cause of sudden death?" J Am Coll Cardiol **41**(2): 329-332.

Yuan, S. M. and H. Jing (2010). "Marfan's syndrome: an overview." Sao Paulo Med J **128**(6): 360-366.

Zhou, Y., M. H. Poczatek, K. H. Berecek and J. E. Murphy-Ullrich (2006). "Thrombospondin 1 mediates angiotensin II induction of TGF-beta activation by cardiac and renal cells under both high and low glucose conditions." Biochem Biophys Res Commun **339**(2): 633-641.

Zhou, Y. Q., F. S. Foster, B. J. Nieman, L. Davidson, X. J. Chen and R. M. Henkelman (2004). "Comprehensive transthoracic cardiac imaging in mice using ultrasound biomicroscopy with anatomical confirmation by magnetic resonance imaging." Physiol Genomics **18**(2): 232-244.